

## OBSERVATIONAL EVIDENCE FOR A DARK SIDE TO NGC 5128’S GLOBULAR CLUSTER SYSTEM<sup>†</sup>

MATTHEW A. TAYLOR<sup>1,2,\*</sup>, THOMAS H. PUZIA<sup>1</sup>, MATIAS GOMEZ<sup>3</sup>, KRISTIN A. WOODLEY<sup>4</sup>

<sup>1</sup>Institute of Astrophysics, Pontificia Universidad Católica de Chile, Av. Vicuña Mackenna 4860, 7820436 Macul, Santiago, Chile

<sup>2</sup>European Southern Observatory, Alonso de Cordova 3107, Vitacura, Santiago, Chile

<sup>3</sup>Departamento de Ciencias Físicas, Universidad Andres Bello, República 220, Santiago, Chile

<sup>4</sup>University of California, Santa Cruz, University of California Observatories, 1156 High Street, Santa Cruz, CA 95064, USA

*Submitted to The Astrophysical Journal*

### ABSTRACT

We present a study of the dynamical properties of 125 compact stellar systems (CSSs) in the nearby giant elliptical galaxy NGC 5128, using high-resolution spectra ( $R \approx 26\,000$ ) obtained with VLT/FLAMES. Our results provide evidence for a new type of star cluster, based on the CSS dynamical mass scaling relations. All radial velocity ( $v_r$ ) and line-of-sight velocity dispersion ( $\sigma_{\text{los}}$ ) measurements are performed with the penalized pixel fitting (*ppxf*) technique, which provided  $\sigma_{\text{ppxf}}$  estimates for 115 targets. The  $\sigma_{\text{ppxf}}$  estimates are corrected to the 2D projected half-light radii,  $\sigma_{1/2}$ , as well as the cluster cores,  $\sigma_0$ , accounting for observational/aperture effects and are combined with structural parameters, from high spatial resolution imaging, in order to derive total dynamical masses ( $M_{\text{dyn}}$ ) for 112 members of NGC 5128’s star cluster system. In total, 89 CSSs have dynamical masses measured for the first time along with the corresponding dynamical mass-to-light ratios ( $\Upsilon_V^{\text{dyn}}$ ). We find two distinct sequences in the  $\Upsilon_V^{\text{dyn}}-M_{\text{dyn}}$  plane, which are well approximated by power laws of the forms  $\Upsilon_V^{\text{dyn}} \propto M_{\text{dyn}}^{0.33 \pm 0.04}$  and  $\Upsilon_V^{\text{dyn}} \propto M_{\text{dyn}}^{0.79 \pm 0.04}$ . The shallower sequence corresponds to the very bright tail of the globular cluster luminosity function (GCLF), while the steeper relation appears to be populated by a distinct group of objects which require significant dark gravitating components such as central massive black holes and/or exotically concentrated dark matter distributions. This result would suggest that the formation and evolution of these CSSs are markedly different from the “classical” globular clusters in NGC 5128 and the Local Group, despite the fact that these clusters have luminosities similar to the GCLF turn-over magnitude. We include a thorough discussion of myriad factors potentially influencing our measurements.

*Subject headings:* galaxies: individual: (NGC 5128) – galaxies: star clusters: general – galaxies: spectroscopy – galaxies: photometry

### 1. INTRODUCTION

Globular clusters (GCs) are among the oldest stellar systems in the Universe (Krauss & Chaboyer 2003). They have witnessed the earliest stages of star formation and were also present during later epochs of structure formation. Apart from resolved stellar population studies of galaxies, which are restricted primarily to the Local Group, extragalactic globular cluster systems (GCSs) provide one of the best probes to investigate the formation and assembly histories of galaxies (Harris 1991; Ashman & Zepf 1998, 2008; Peng et al. 2008; Georgiev et al. 2010). Various avenues of study can be employed to this effect, including the analysis of GCS kinematics, their metallicity distribution functions, chemical enrichment histories, age spreads, and/or combinations thereof.

At a distance of  $3.8 \pm 0.1$  Mpc, (Harris et al. 2010), corresponding to an angular scale of  $18.5 \text{ pc arcsec}^{-1}$ , NGC 5128 (a.k.a. Centarus A) is the nearest giant elliptical (gE) galaxy to the Milky Way (MW), yet it is still too far for large scale star-by-star investigations to be technologically feasible. Fortunately, much has been learned about this galaxy from its rich GC system. 564 of its GCs have radial velocity confirmations, and others have been confirmed, for example, via resolution into individual stars (van den Bergh et al. 1981; Hesser et al. 1984, 1986; Harris et al. 1992; Peng et al. 2004; Woodley et al. 2005; Rejkuba et al. 2007; Beasley et al. 2008;

Woodley et al. 2010a). This GC sample, thus, rivals the entire population of GCs harbored by the Local Group, despite there being  $\sim 600 - 1400$  GCs still left to find/confirm in the halo regions of NGC 5128 (Harris et al. 1984, 2002b, 2010, 2012). Notwithstanding this incompleteness, previous studies have already shed much light on the photometric, chemical, and kinematical properties, as well as the past and recent formation history of this massive nearby neighbour.

GCs are well known to inhabit a narrow range of space defined by structural parameters such as half-light, tidal and core radii ( $r_h$ ,  $r_t$  and  $r_c$ , respectively), concentration parameter  $c = \log(r_t/r_c)$  (King 1966), velocity dispersion ( $\sigma$ ), mass-to-light ratio ( $\Upsilon$ ), etc. called the “fundamental plane” (Djorgovski 1995). Studies of Local Group GCs (e.g. Fusi Pecci et al. 1994; Djorgovski et al. 1997; Holland et al. 1997; McLaughlin 2000; Barmby et al. 2002, 2007) have shown that at the high-mass end of the fundamental plane, peculiar GCs such as  $\omega$ Cen and G1, the largest GCs in the MW and M31, begin to emerge. For example, both of these GCs show significant star-to-star [Fe/H] variations and are among the most flattened of Local Group GCs (White & Shawl 1987; Norris & Da Costa 1995; Meylan et al. 2001; Pancino et al. 2002) and at least in the case of  $\omega$ Cen, harbor multiple stellar populations with an extended chemical enrichment history (Piotto 2008a,b).

Unlike the Local Group, the sheer size of NGC 5128’s GCS generously samples the high-mass tail ( $\gtrsim 10^6 M_\odot$ ) of the globular cluster mass function (GCMF, Harris et al. 1984, 2002a; Martini & Ho 2004; Rejkuba et al. 2007; Taylor et al. 2010). Due to their intense luminosities, these massive GCs

<sup>†</sup> Based on observations collected under program 081.D-0651 (PI: Matias Gomez) with FLAMES at the Very Large Telescope of the Paranal Observatory in Chile, operated by the European Southern Observatory (ESO).

\* ESO Graduate Student Fellow, *mataylor@astro.puc.cl*

are very accessible observationally, and thus provide excellent probes to study the formation history of NGC 5128. Many of the most massive NGC 5128 GCs show a more rapid chemical enrichment history than Local Group GCs (Colucci et al. 2013), and exhibit significantly elevated dynamical mass-to-light ratios ( $\Upsilon_V^{\text{dyn}}$ ) above dynamical masses,  $\mathcal{M}_{\text{dyn}} \simeq 2 \cdot 10^6 M_{\odot}$  (Taylor et al. 2010). This sharp upturn of  $\Upsilon_V^{\text{dyn}}$  is consistent with a trend found by Hasegan et al. (2005) and Mieske et al. (2006, 2008a) in other extragalactic GCSs, and requires either non-equilibrium dynamical states, such as rotation or pre-relaxation (Varri & Bertin 2012; Bianchini et al. 2013), younger than expected stellar components (e.g. Bedin et al. 2004; Piotto 2008a), exotic top- or bottom-heavy stellar initial mass functions (IMFs; e.g. Dabringhausen et al. 2008, 2009; Mieske et al. 2008b) or/and a significant contribution by non-baryonic matter or massive central black holes (BHs). While there is an ongoing debate whether the latter two options are valid for Milky Way GCs (see e.g. Conroy et al. 2011; Ibata et al. 2013; Lützgendorf et al. 2011; Strader et al. 2012; Lanzoni et al. 2013; Sun et al. 2013; Kruijssen & Lützgendorf 2013), there is growing evidence for the presence of  $10^5 - 10^8 M_{\odot}$  BHs significantly affecting the dynamics of similarly structured, albeit more massive, ultra-compact dwarf galaxies (UCDs; Mieske et al. 2013; Seth et al. 2014).

NGC 5128's GCS has been shown to follow trends similar to other giant galaxies. In particular, it has a multimodal distribution in color and metallicity (e.g. Harris et al. 2002b; Peng et al. 2004; Beasley et al. 2008; Woodley et al. 2010b), corresponding to at least two and possibly three distinct GC generations. Moreover, the prominent dust-lane and faint shells in the galaxy surface brightness distribution (Malin et al. 1983), along with a young tidal stream (Peng et al. 2002) provide significant evidence for recent merger activity on a kpc scale, while on smaller scales indications of strong tidal forces are seen in the form of extra-tidal light associated with individual GCs (Harris et al. 2002a).

Recent models support the notion that the bulk of the star formation leading to massive elliptical galaxies is complete by  $z \approx 3$  (i.e. the first few Gyr of cosmic history), while it takes until  $z < 0.4$  before  $\sim 80\%$  of the mass is locked up after the accretion of as many as five massive progenitors (e.g. De Lucia et al. 2006; De Lucia & Blaizot 2007; Marchesini et al. 2014). Studies based on *Hubble Space Telescope* (HST) data in the mid- to outer-halo regions of NGC 5128 generally concur with this view, in that the majority ( $\sim 80\%$ ) of the stellar population is ancient ( $\gtrsim 11-12$  Gyr) and formed very rapidly, as evidenced by  $[\alpha/\text{Fe}]$  ratios approaching or exceeding twice solar values (e.g. Harris et al. 1999; Harris & Harris 2000, 2002; Rejkuba et al. 2011). This older population is complemented by a significantly younger component, forming on the order of a few Gyr ago (e.g. Soria et al. 1996; Marleau et al. 2000; Rejkuba et al. 2003).

In this paper we use velocity dispersion estimates based on high-resolution spectra to derive dynamical masses for a large sample of NGC 5128's GCS (see e.g., Chilingarian et al. 2011, who carried out similar work on ultra-compact dwarfs in the Fornax cluster). We combine the newly derived dynamical information with well-known luminosities from the literature to probe the baryonic makeup and dynamical configurations of the CSSs. The results are then used to classify several distinct CSS/GC populations, which are discussed in the context of likely origins, with potential consequences for GCSs that surround other gE galaxies.

This paper is organized as follows. § 2 describes the observations made as well as an outline of the data reduction steps taken to produce high-quality spectra. § 3 contains information on the analysis that was undertaken on the new spectroscopic observations, as well as structural parameter data from the literature with which our new measurements were combined. § 4 discusses our results by using sizes, masses and mass-to-light ratios of GCs/CSSs to develop several hypotheses on the origins of the various cluster sub-populations that we find. The main text concludes with § 5, which summarizes our new measurements and results. Following the main text, we present in the appendix multiple detailed tests which rule out spurious results due to several possible sources including poor data quality, data analysis biases, fore/background contamination, target confusion, and others. We adopt the NGC 5128 distance modulus of  $(m - M)_0 = 27.88 \pm 0.05$  mag, corresponding to a distance of  $3.8 \pm 0.1$  Mpc (Harris et al. 2010), as well as the homogenized GC identification scheme of Woodley et al. (2007) throughout this work.

## 2. OBSERVATIONS

During five nights in June/July 2008, 123 of the brightest GCs around NGC 5128 were observed using the Fibre Large Array Multi-Element Spectrograph (FLAMES) instrument at the Very Large Telescope (VLT) on Cerro Paranal, Chile. FLAMES is a multi-object spectrograph mounted at the Nasmyth A focus of UT2 (Kueyen). The instrument features 132 fibres, each with apertures of  $1.2''$  diameter, linked to the intermediate-high resolution ( $7\,000 \leq R \leq 30\,000$ ) GIRAFFE spectrograph, with an additional eight  $1.0''$  fibres connected to the high resolution ( $R \approx 47\,000$ ) UVES spectrograph mounted at the Nasmyth B focus, thus, allowing for simultaneous observations of 139 targets<sup>3</sup> over a  $25'$  diameter field of view.

### 2.1. Instrumental Setup

FLAMES often suffers from one or more broken fibres, and these observations were no exception. The first night of observations, comprising the first three of eleven 2 400 second long observing blocks (OBs), were conducted with the first of two FLAMES fibre positioner plates, which suffered from two broken fibres, while the last eight OBs used the second plate, with only a single, but distinct, broken fibre. For this reason, the total number of targets observed was 138, including eight fibres fed to UVES, and 130 to GIRAFFE. Unfortunately the UVES targets were of too low data quality for useful measurements to be derived, and so we do not include them in the present work. From the GIRAFFE fibre budget, 13 were allocated to recording the sky contribution to the target signals. These sky fibres were used near the end of the data reduction process to perform an adaptive sky subtraction. In summary, we obtained spectra of 117 bright GCs using GIRAFFE in the high resolution ( $R \simeq 25\,900$ ) mode, recording a single  $\Delta\lambda = 21.3$  nm echelle order centred at  $\lambda = 525.8$  nm, covering the wavelength range  $515.2 \lesssim \lambda \lesssim 536.5$  nm.

Table 1 summarizes our observations. The overall exposure times were 26 400 s; however, three GCs (GC 0310, GC 0316 and GC 426) inevitably suffered from broken fibres, limiting the total integration times to 19 200 s, 7 200 s, and 7 200 s, respectively. In the case of GC 0058 a single exposure had to be omitted due to the unfortunate coincidence of a significant

<sup>3</sup> In principle 132 GIRAFFE fibres are allocatable, but only 131 are fully covered on the detector; therefore, the sum of GIRAFFE+UVES available fibres is 139.

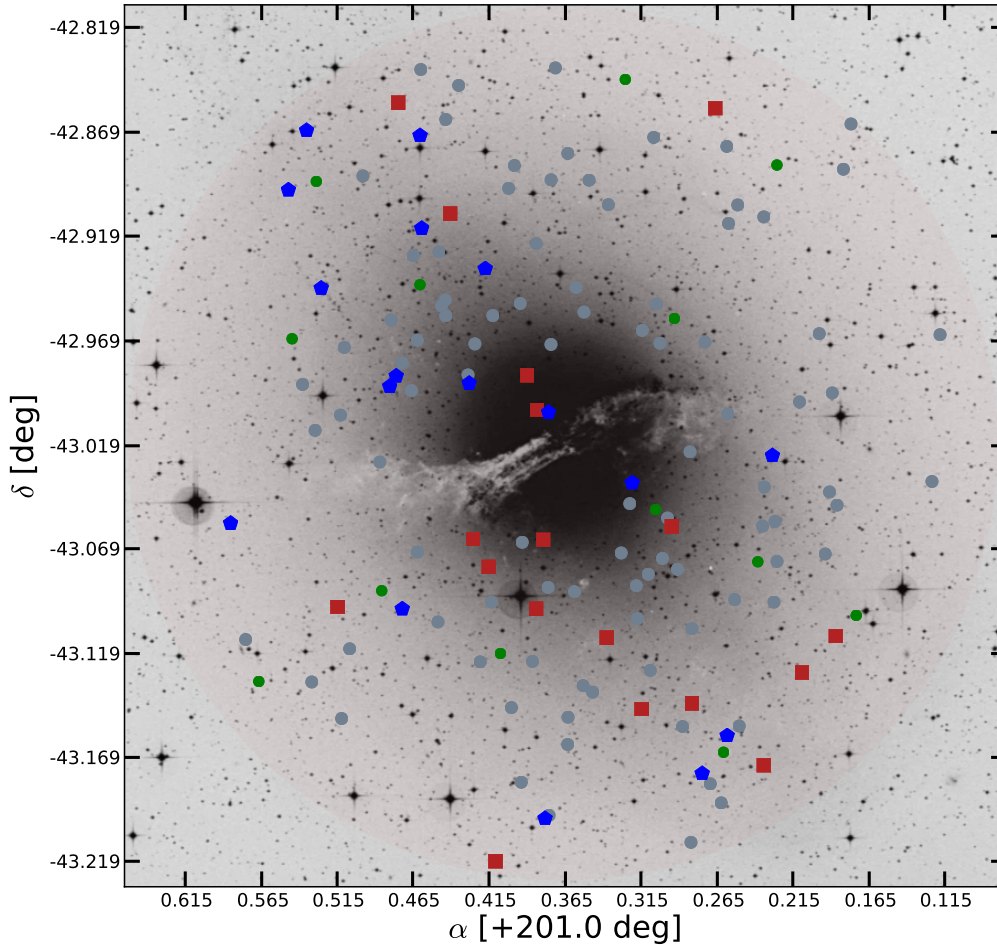


FIG. 1.— Locations of the GIRAFFE fibre placements in relation to the host galaxy, NGC 5128. Grey points show the placement of fibres for “classical” GCs, while blue pentagons and red squares illustrate the positions of DGTO and DSC GCs, respectively (see Figure 6 and corresponding text in Sect. 4.1 for details on their definition). Green points mark the positions of sky fibres. The light red shaded region shows the approximate extent of the 25’ FLAMES field-of-view, corresponding to  $\sim 27.5$  kpc at the distance of NGC 5128.

detector defect lying directly in the middle of the  $Mgb$  triplet, hence the total integration time for that GC was limited to 24 000 s.

The on-sky locations of the GIRAFFE fibres are indicated in Figure 1, over-plotted on an archival DSS image<sup>4</sup> of NGC 5128. Overall, the observing conditions were good for this observing program: The images were taken at airmass values ranging between 1.054 and 1.635, under seeing conditions in the range  $0.48''$  to  $1.42''$ . For the purpose of correcting our line-of-sight velocity dispersion measurements, based on our final stacked spectra, for aperture and observational effects (see § 3.5), we use the mean seeing value from all 11

OBs of  $0.85''$ , since all targets were observed simultaneously under identical seeing conditions.

## 2.2. Basic Data Reduction and Cleaning

The basic data reduction steps (bias subtraction, flat fielding, and wavelength calibration) were carried out by the GIRAFFE pipeline<sup>5</sup>. Separate calibration frame sets were used for each of the five nights. The pipeline recipe *masterbias* created the master bias frame from an average of five individual frames and *masterflat* produced the master flat from an average of three bias-subtracted flatfields. The fibre localizations were visually confirmed to be accurate to within 0.5 pixels for each of the 11 OBs, less than the suggested 1 pixel maximum to ensure accuracy. The recipe *giwavecalibration* derived the wavelength calibrations. For all five calibration sets, it was necessary to edit the slit geometry tables in order to eliminate ‘jumps’ in the final, re-binned, wavelength calibrated arc-lamp spectra – an extra step that is not uncom-

<sup>4</sup> Based on photographic data obtained using The UK Schmidt Telescope. The UK Schmidt Telescope was operated by the Royal Observatory Edinburgh, with funding from the UK Science and Engineering Research Council, until 1988 June, and thereafter by the Anglo-Australian Observatory. Original plate material is copyright © the Royal Observatory Edinburgh and the Anglo-Australian Observatory. The plates were processed into the present compressed digital form with their permission. The Digitized Sky Survey was produced at the Space Telescope Science Institute under US Government grant NAG W-2166.

<sup>5</sup> <http://www.eso.org/sci/software/pipelines>

TABLE 1  
 STAR CLUSTER OBSERVATIONS

ID	$\alpha$ [J2000]	$\delta$ [J2000]	$R$ [mag]	$V_0$ [mag]	Exp. Time [s]	S/N
GC 0028	13 24 28.429	-42 57 52.96	19.65	19.80±0.01	26400	2.87
GC 0031	13 24 29.700	-43 02 06.43	19.55	19.75±0.01	26400	1.88
GC 0048	13 24 43.586	-42 53 07.22	19.33	19.51±0.01	26400	1.79
GC 0050	13 24 44.575	-43 02 47.26	18.90	18.74±0.01	26400	3.75
GC 0052	13 24 45.330	-42 59 33.47	18.91	18.98±0.01	26400	5.55
GC 0053	13 24 45.754	-43 02 24.50	19.43	19.57±0.01	26400	2.22
GC 0054	13 24 46.435	-43 04 11.60	18.64	18.84±0.01	26400	4.65
GC 0058	13 24 47.369	-42 57 51.19	19.15	19.41±0.01	24000	2.69
GC 0064	13 24 50.072	-43 07 36.23	20.03	20.11±0.02	26400	1.49
GC 0065	13 24 50.457	-42 59 48.98	19.68	19.21±0.01	26400	2.17

NOTE. — Summary of the new observations. Cluster identifications are listed in the first column, followed by the J2000 coordinates, apparent  $R$ -band magnitudes used for target acquisitions, de-reddened apparent  $V$ - or  $r'$ -band magnitudes (see §3.6), total integration times, and signal-to-noise ratios (S/N, see Sect. 2.2 for a definition). Table 1 is published in its entirety in the electronic edition of the *Astrophysical Journal*. A portion is shown here for guidance regarding its form and content.

mon. Having performed these steps, the wavelength solutions were confirmed to be of high-quality by visually checking that they were smooth, as well as via the radial velocity errors internal to the re-made slit geometry tables which showed values of  $RVERR \simeq 0.003 \text{ km s}^{-1}$ . We note that these values are meant to confirm the accuracy of *giwavecalibration* and do not reflect our final, measured radial velocity uncertainties (see § 3).

Using the final 11 sets of calibration data products, the recipe *giscience* provided the final, fully calibrated science frames from which individual 1D spectra were extracted. Custom PYTHON scripts were used to clean the spectra of numerous residual cosmetic defects and to subtract the sky contribution from the spectra. To clean the spectra of cosmetic defects surviving the basic data reduction steps, the spectra were subjected to a median filtering algorithm and robust  $\kappa\sigma$ -clipping. Each of the extracted spectra were visually inspected and the parameters of the median/ $\kappa\sigma$  filters were adjusted to remove any significant detector cosmetics, while preserving the finer details of the spectra. Typically a median filter of gate size of 75 pixels followed by clipping points outside of  $4.5\sigma$  was sufficient to remove defects.

### 2.3. Sky Subtraction

To account for the sky contribution to each spectrum, we used the 13 GIRAFFE fibres dedicated to monitoring the sky contamination. These fibres facilitated uniform sampling across the field of view (see Figure 1). For each target, the sky contribution was taken to be the average of the three nearest sky fibres, inversely weighted by distance, thereby ensuring that only the sky nearest to each target was considered. The final sky spectra were determined individually for each of the 117 targets and 11 OBs before being directly subtracted from each of the 1287 individual target spectra. Only then were the reduced, cleaned, and sky-subtracted spectra co-added to produce the final data set.

### 2.4. Data Quality Assessment

The signal-to-noise ratios (S/N) for the final spectra were calculated considering the main spectral features used to estimate the line-of-sight velocity dispersions (see §3.1). Specifically, these features are the Mgb and Fe 5270 Lick indices centred at laboratory wavelengths of  $5176.375 \text{ \AA}$  and  $5265.650 \text{ \AA}$ , respectively (Burstein et al. 1984; Worthey 1994; Worthey &

Ottaviani 1997). The S/N listed in Table 1 were calculated as,

$$S/N = \frac{1}{4} \sum_i^4 \frac{s_i}{\sigma_i} \quad (1)$$

where  $s_i$  and  $\sigma_i$  are the mean and standard deviation of the flux over the continuum regions bracing the Mgb and Fe 5270 features as defined by  $5142.625 \text{ \AA} \leq \lambda_{\text{Mgb,cont}}^{\text{blue}} \leq 5161.375 \text{ \AA}$ ,  $5191.375 \text{ \AA} \leq \lambda_{\text{Mgb,cont}}^{\text{red}} \leq 5206.375 \text{ \AA}$ ,  $5233.150 \text{ \AA} \leq \lambda_{\text{Fe5270,cont}}^{\text{blue}} \leq 5248.150 \text{ \AA}$  and  $5285.650 \text{ \AA} \leq \lambda_{\text{Fe5270,cont}}^{\text{red}} \leq 5318.150 \text{ \AA}$ . Before calculating the S/N, each of the continuum definitions were shifted from the laboratory values to account for known GC radial velocities,  $v_r$ , or if unknown, they were shifted *a posteriori* according to our own  $v_r$  measurements (see § 3.1).

## 3. ANALYSIS

### 3.1. Penalized Pixel Fitting

Our line-of-sight velocity dispersion (LOSVD;  $\sigma$ ) measurements were carried out using the penalized pixel fitting (*ppxf*) code (Cappellari & Emsellem 2004). This code parametrically recovers the LOSVD of the stars composing a given cluster or galaxy spectrum by expanding the LOSVD profile as a Gauss-Hermite series. Using reasonable initial guesses for the radial velocity ( $v_r$ ) and  $\sigma$ , the best fitting  $v_{r,\text{ppxf}}$ ,  $\sigma_{\text{ppxf}}$ , and Hermite moments  $h_3$ , and  $h_4$  were recovered by fitting the cluster/galaxy spectrum to a library of template stars which had its spectral resolution adjusted to that of the FLAMES spectra. The fitting of optimal template spectra along with the kinematics serves to limit the impact of template mismatches. An important feature of the *ppxf* routine is that during an iterative process, a penalty function derived from the integrated square deviation of the line profile from the best fitting Gaussian is used to minimize the variance of the fit. This feature allows the code to recover the higher order details in high S/N spectra, but biases the solution towards a Gaussian when S/N is low, as is the case for several objects in our sample. For more details on the *ppxf* code, we refer to Cappellari & Emsellem (2004)<sup>6</sup>.

Where possible, the input estimates for  $v_r$  were quoted from Woodley et al. (2010a) or Woodley et al. (2007) which are

<sup>6</sup> *ppxf* and the corresponding documentation can be found at: <http://www-astro.physics.ox.ac.uk/~mxc/idl/>

listed in Table 2. For GCs with unavailable  $v_r$ , we used the IRAF<sup>7</sup> task *rvcorrect* to account for heliocentric velocity corrections, and *fxcor* to estimate  $v_r$ . These estimates were used as our initial guesses for *ppxf* and do not need to be perfectly accurate since the  $\sigma_{\text{ppxf}}$  measurements have no significant sensitivity to  $v_r$ , as long as the initial guess is accurate to within a few tens of  $\text{km s}^{-1}$  (see also Taylor et al. 2010). The more refined  $v_{r,\text{ppxf}}$  values were then adopted as our final estimates as listed in Table 2 and used for our S/N measurements.

To account for any sensitivity that *ppxf* may have to the initial guess for  $\sigma$  which may, for example, result in spurious solutions, we varied the input  $\sigma$  between 5 and  $100 \text{ km s}^{-1}$  in steps of  $1 \text{ km s}^{-1}$  for each spectrum. For each fit we used the entire  $5152 \lesssim \lambda/\text{\AA} \lesssim 5365$  range, including the Mgb and Fe features and **all less prominent lines that are present**. All GIRAFFE spectra have a velocity scale of  $2.87 \text{ km s}^{-1}$ , and we found an additive 4<sup>th</sup> degree polynomial adequate for the purpose of estimating the continua. After varying our initial  $\sigma$  guesses, the adopted  $v_{r,\text{ppxf}}$  and  $\sigma_{\text{ppxf}}$  values correspond to the mean of the output sets of  $v_{r,\text{ppxf}}$  and  $\sigma_{\text{ppxf}}$  after being  $\kappa\sigma$ -clipped to remove outliers. The *ppxf* errors were taken as the mean of the output *ppxf* errors added in quadrature to one standard deviation of the  $\kappa\sigma$ -clipped results. While it is too cumbersome to present all of the *ppxf* fits in the present work, we direct the reader to the online-only appendix<sup>8</sup> to access the full suite of spectral fits for all targets in this sample and present a representative sample in Figure 2.

### 3.2. Template Library

The *ppxf* code measurements rely on a library of template stellar spectra capable of accurately replicating an integrated light spectrum when used in combination and Doppler shifted to account for velocity gradients within a stellar population. We used a library of high-resolution synthetic spectra from the PHOENIX<sup>9</sup> collaboration (Husser et al. 2013). A synthetic spectral library was chosen over observed templates because current high resolution observed spectral libraries do not cover the wide range of stellar parameters that comprise complex stellar populations. We therefore used a library of 1 100 PHOENIX spectra covering the stellar parameter ranges:  $0.5 \leq \log g \leq 4.0$ ,  $3800 \leq T_{\text{eff}} \leq 6000 \text{ K}$ ,  $-4.0 \leq [\text{Fe}/\text{H}] \leq +1.0 \text{ dex}$ , and  $-0.2 \leq [\alpha/\text{Fe}] \leq +1.2 \text{ dex}$ . For  $[\text{Fe}/\text{H}] = -4.0$  and  $[\text{Fe}/\text{H}] = +1.0$ . The PHOENIX spectra are available only for  $[\alpha/\text{Fe}] = 0.0 \text{ dex}$ ; however, we do not expect that this limitation affects our results significantly.

### 3.3. Comparison with Previous Results

The accuracy of *ppxf* when applied to the restricted  $\sim 200 \text{ \AA}$  GIRAFFE wavelength coverage was tested by using the GC spectra of Taylor et al. (2010) as a comparison sample since they also derived LOSVD estimates in the same manner, but with much wider spectral coverage. To compare directly, the Taylor et al. spectra were constrained to the GIRAFFE wavelength range, and  $\sigma_{\text{ppxf}}$  estimates were obtained as described in the following. The input values for  $v_r$  and  $\sigma$  were fixed at those determined by Taylor et al., and the input  $\sigma$  were varied around the known values by  $\pm 10 \text{ km s}^{-1}$  in steps of 1

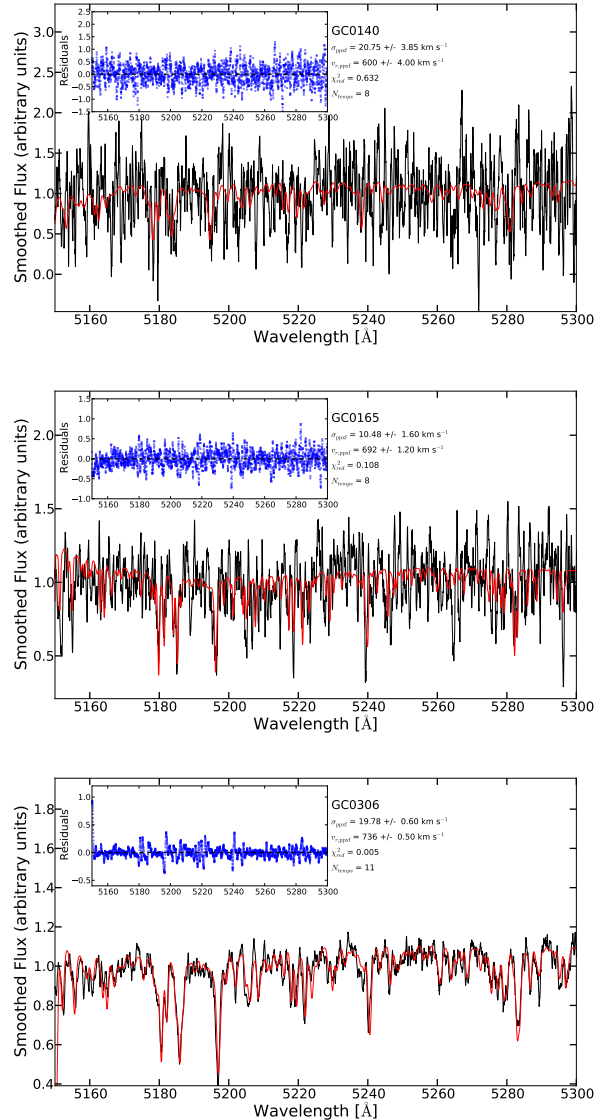


FIG. 2.— Examples of the *ppxf* spectral fits (red lines) from a low-quality (top) to a high-quality spectrum (bottom). The reduced spectra (black lines) have been smoothed with a box size of 8 pixels, representative of the instrumental FWHM of GIRAFFE. The inset blue plots show the residuals, beside which we list some output information for each target. From top to bottom this information is the GC identification, our adopted  $\sigma_{\text{ppxf}}$ ,  $v_{r,\text{ppxf}}$ , reduced  $\chi^2$ , and the number of template spectra used in their calculation.

$\text{km s}^{-1}$ . The output values for  $\sigma$  and  $v_r$  are averaged and plotted as a function of input values in Figure 3 for comparison.

The top panel of Figure 3 shows that the agreement for  $\sigma_{\text{ppxf}}$  is generally good, with most of the GCs clustering around the unity relation. The results of one GC (GC 0382) are not shown, as our new LOSVD value of  $178.77 \pm 7.58 \text{ km s}^{-1}$  is unlikely to be reliable considering that it implies a dynamical mass of  $\sim 10^9 M_{\odot}$  within a half-light radius of  $\sim 2 \text{ pc}$ . Given that GC 0382 has three independent  $v_r$  measurements confirming it to be a member of NGC 5128 (Woodley et al. 2010a, and the present work), and thus not a fore/background source, we adopt Taylor et al.'s  $\sigma_{\text{ppxf}} = 14.3 \pm 3.2 \text{ km s}^{-1}$  for the rest of the analysis. The few other outliers in Figure 3 correspond to the former study's most uncertain GCs, so we prefer our  $\sigma_{\text{ppxf}}$  estimates since our template library has a significantly wider range of stellar param-

<sup>7</sup> IRAF is distributed by the National Optical Astronomy Observatory, which is operated by the Association of Universities for Research in Astronomy, Inc., under cooperative agreement with the National Science Foundation.

<sup>8</sup> <http://cdsarc.u-strasbg.fr/viz-bin/Cat/>

<sup>9</sup> <http://phoenix.astro.physik.uni-goettingen.de/>

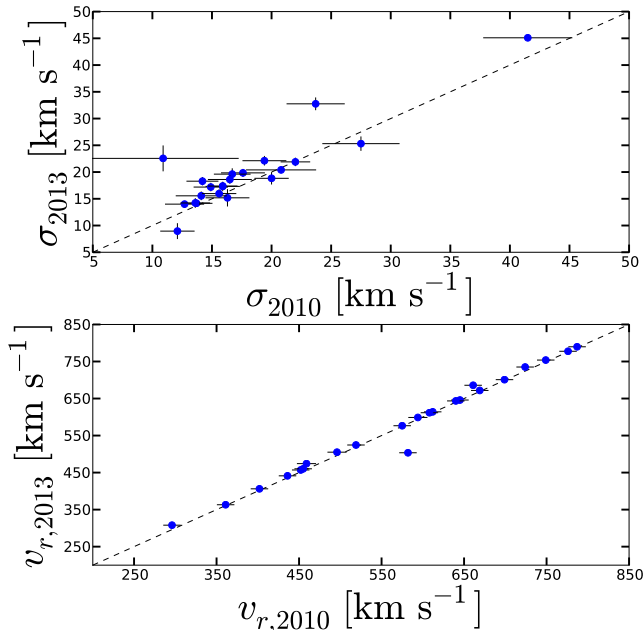


FIG. 3.— Comparison of the *ppxf* accuracy using the GC sample of Taylor et al. (2010) when the spectral range is restricted to that of the GIRAFFE spectra used in this work. The upper panel shows the  $\sigma$  comparison and the lower panel shows the same for  $v_r$ . In both panels, the Taylor et al. (2010) results are shown along the x-axes and the new results are shown along the y-axes. Unity relations are indicated as dashed lines.

eters and much higher S/N ratio over the wavelength range used to estimate  $v_{r,\text{ppxf}}$  and  $\sigma_{\text{ppxf}}$ . Meanwhile, the bottom panel shows that the agreement in  $v_{r,\text{ppxf}}$  is excellent, with the scatter around the unity relation being consistent with the measurement uncertainties. The significant outlier corresponds to GC 0382, which we consider to be unreliable and defer to any previously derived  $v_r$  estimates in the literature.

Our new  $v_{r,\text{ppxf}}$  estimates are listed in column four of Table 2, compared to literature values listed in column three. We note that GC 0218, GC 0219, GC 0228 have  $v_r$  measured for the first time ( $528 \pm 1.90 \text{ km s}^{-1}$ ,  $661 \pm 2.70 \text{ km s}^{-1}$  and  $478 \pm 19.40 \text{ km s}^{-1}$ , respectively), all consistent with the  $541 \text{ km s}^{-1}$  systemic velocity of NGC 5128 (Woodley et al. 2010a). There were 15 GCs for which *ppxf* was unable to provide  $v_r$  estimates, including GC 0261 and GC 0315, leaving them still as  $v_r$  unconfirmed members of NGC 5128. Thus, Table 2 lists new accurate  $v_r$  estimates for 125 NGC 5128 GCs, including three first-time measurements.

We compare the new  $v_{r,\text{ppxf}}$  estimates to literature radial velocities ( $v_{r,\text{lit}}$ ) in Figure 4 where  $v_{r,\text{lit}}$  and  $v_{r,\text{ppxf}}$  are shown along the  $x$ - and  $y$ -axes, respectively. The Woodley et al. (2007) and Woodley et al. (2010a) catalogues provide the most comprehensive collections of NGC 5128 GC radial velocities to date. For the comparison we adopt the weighted-average values listed in Woodley et al. (2010a) where possible. If there exists only a single Woodley et al. (2010a) value measured from an individual spectrum, then we adopt the Woodley et al. (2007) estimates, unless the former agrees significantly better with our new measurements. Figure 4 shows generally good agreement within the literature uncertainties, with a single notable exception being GC 0095. For this GC, we prefer the literature measurement of  $v_{r,\text{lit}} = 374 \pm 34 \text{ km s}^{-1}$  over our  $\sigma_{\text{ppxf}} = 826 \pm 7.8 \text{ km s}^{-1}$  because visual inspection of the corresponding Doppler shifts shows

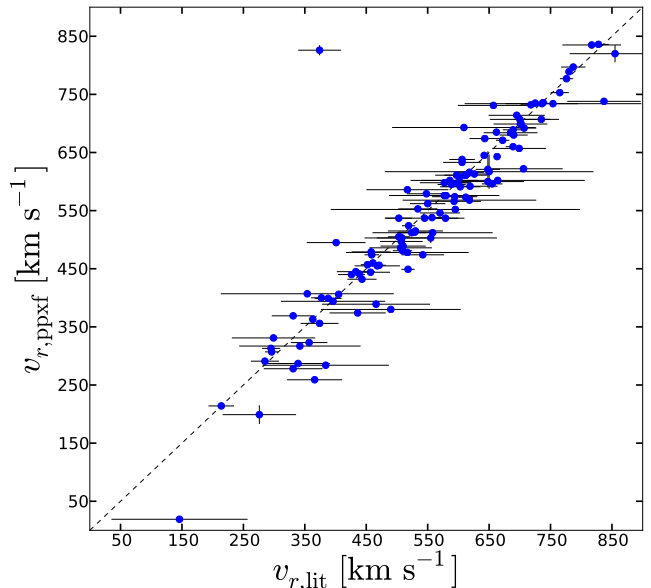


FIG. 4.— Comparison between the radial velocities newly estimated by *ppxf*,  $v_{r,\text{ppxf}}$  to those previously measured from the literature,  $v_{r,\text{lit}}$ . The comparison is generally good, as indicated by the dashed line showing the unity relation. However, our measurements are in most cases of significantly higher quality, as illustrated by the  $v_{r,\text{ppxf}}$  error bars, which for our dataset are often on the order of or smaller than the symbol size.

better agreement with the laboratory wavelengths of the spectral absorption features when using the former value. Given this discrepancy, and the resulting uncertainty of the derived  $\sigma_{\text{ppxf}}$ , we drop this object from the analysis. In any other case where  $v_r$  are discrepant we prefer our  $v_{r,\text{ppxf}}$  due to smaller uncertainties.

Despite obtaining reliable  $v_r$  estimates for almost all of our targets, there were 25 GCs for which we consider  $\sigma_{\text{ppxf}}$  to be unreliable either due to uncomfortably large error bars, or simply a failure to derive an estimate at all. We therefore drop these targets from the subsequent analysis and carry on with the remaining 115 new  $\sigma_{\text{ppxf}}$  estimates, including the re-analyzed Taylor et al. GCs.

### 3.4. Structural Parameters

We took 2D projected half-light radii,  $r_h$ , and concentration parameters,  $c$ , from the three sources as listed in Table 3. The majority of the values listed for  $r_h$  and  $c$  are, where available, from Jordán et al. (2015, *in prep.*), based on *HST* data, and are otherwise taken from Gomez et al. (2015, *in prep.*) based on *IMACS* data taken under exceptional seeing ( $\lesssim 0.5''$ ). Despite the sub-arcsecond seeing conditions, the marginally resolved nature of most GCs did not allow for accurate  $c$  estimates by Gomez et al., so for many, a typical value of 1.48 was assigned. Moreover, three extremely small *IMACS*-based  $r_h$  estimates exist where there is no *HST* imaging available; however, these GCs (GC 0085, 0333, 0429) are not resolved in the images and thus we drop them from the analysis and continue with the remaining 112 CSSs. The re-analyzed clusters of Taylor et al. (2010) use the same parameters as in that paper, namely those derived in Harris et al. (2002a). For the latter GCs, the  $r_h$  errors listed are adopted from the same paper. At the time of writing, no errors were available for the Gomez et al. and Jordán et al. sizes, so for these clusters we adopt values of 0.43 pc, which is the average size error of the

Taylor et al. (2010) sample, and while representative for the new *HST* measurements, may underestimate the *IMACS* errors. Following Harris et al. (2002a), we assume 0.15 for the errors on all  $c$ , noting that these probably underestimate the true *IMACS*-based measurement errors as well. In any case, although assigning error estimates in this manner is not optimal, we do not expect it to affect our main results significantly given the dominance of  $\sigma$  on the uncertainties of our dynamical mass estimates (see § 3.6).

### 3.5. Aperture Corrections

The  $\sigma_{\text{ppxf}}$  values listed in Table 2, while generally accurate, are not appropriate to use when estimating dynamical masses. Several effects, both observational (seeing, target distance, etc.) and instrumental (spectral/spatial resolution, sampling, etc.), may conspire to affect how representative the light entering a given fibre aperture may be of objects similar to massive GCs and UCDs (Mieske et al. 2008a). In our case the 1.2'' diameters of the FLAMES fibres correspond to  $\sim 22$  pc at the distance of NGC 5128, so contributions from stars outside of the core region may skew the  $\sigma_{\text{ppxf}}$  measurements to lower values compared to  $\sigma$  estimates corresponding to smaller radii. Here we describe our approach to correct our measured  $\sigma_{\text{ppxf}}$  estimates to values representing both the GC core regions ( $\sigma_0$ ) and  $\sigma$  values within the GC half-light radius ( $\sigma_{1/2}$ ).

We used the cluster modeling code of Hilker et al. (2007), described in detail in Mieske et al. (2008a), to correct for any aperture effects and determine estimates of  $\sigma_0$  and  $\sigma_{1/2}$  based on our measured  $\sigma_{\text{ppxf}}$ . This code uses the basic structural data (in our case  $r_h$  and  $c$ ) that defines a cluster’s light-profile to generate a 3D King (1966) stellar density profile from which an N-body representation of the cluster is created in 6D (position, velocity) space. Each simulated particle is convolved with a Gaussian corresponding to the true seeing FWHM (see § 2) and a light profile is generated from which the velocity dispersion profile can be obtained.

Using this code, we modeled each of our clusters with  $10^5$  particles and binned them radially in groups of  $10^3$ . The 3D velocity information of each subgroup was used to derive  $\sigma$  profiles according to  $\langle v \rangle_{3D}^2 = 3\sigma^2$  where  $\langle v \rangle_{3D}^2$  is the square of the mean of the 3D velocities. To account for the inherent stochasticity of the modeling, the median of the inner-most five subgroups, or 5% of the modeled stellar population, was adopted as  $\sigma_0$ , while all particles inwards of  $r_h$  were used to calculate  $\sigma_{1/2}$  for each GC. This process was repeated three times per GC. The first set of models used the measured  $\sigma_{\text{ppxf}}$ ,  $r_h$ , and  $c$  as inputs to provide our adopted  $\sigma_0$  and  $\sigma_{1/2}$ , while for the other two iterations we added or subtracted the errors for the three quantities in order to maximize or minimize the modeled  $\sigma$  estimates, respectively. We then adopted the differences between the upper/lower bounds and the output  $\sigma$  values as the corresponding errors. Table 2 lists the resulting  $\sigma_0$  and  $\sigma_{1/2}$  estimates including our uncertainties (columns 8 and 9), alongside the model velocity dispersions corresponding to the FLAMES apertures ( $\sigma_{m,ap}$ ) and the global values ( $\sigma_{m,gl}$ ). The accuracy of the code is verified by the very good agreement between the predicted  $\sigma_{\text{ppxf}}$  and measured  $\sigma_{m,ap}$  at the fibre aperture size.

### 3.6. Star Cluster Masses and Mass-to-Light Ratios

One of the most direct methods to estimate the dynamical mass ( $\mathcal{M}_{\text{dyn}}$ ) of a single-component compact stellar system is by the use of the scalar virial theorem (e.g. Binney

& Tremaine 1987) of the form originally derived by Spitzer (1969),

$$\mathcal{M}_{\text{dyn}} \simeq 2.5 \frac{3\sigma_0^2 r_h}{G} \simeq 1743 \left( \frac{\sigma_0^2}{\text{km}^2 \text{ s}^{-2}} \right) \left( \frac{r_h}{\text{pc}} \right) M_\odot \quad (2)$$

if one assumes a dynamically relaxed cluster, sphericity, and isotropic stellar orbits. While this is among the most commonly used dynamical mass estimators, it has been shown that the “half-mass” ( $\mathcal{M}_{1/2}$ ) or in other words the dynamical mass corresponding to that contained within the 2D projected half-light radius is more robust against stellar velocity dispersion anisotropy. This feature makes  $\mathcal{M}_{1/2}$  an overall more robust mass estimator for dispersion supported systems. We estimate  $\mathcal{M}_{1/2}$  via the form derived by Wolf et al. (2010),

$$\mathcal{M}_{1/2} = 4 \frac{\langle \sigma_{\text{los}}^2 \rangle r_h}{G} \simeq 930 \left( \frac{\langle \sigma_{\text{los}}^2 \rangle}{\text{km}^2 \text{ s}^{-2}} \right) \left( \frac{r_h}{\text{pc}} \right) M_\odot \quad (3)$$

where  $\sigma_{\text{los}}$  is the luminosity-weighted LOSVD, in our case aperture corrected to  $\sigma_{1/2}$ .

Applying Equation 3 to all the GCs with available  $\sigma_{1/2}$ ,  $r_h$ , and  $c$  provides  $\mathcal{M}_{1/2}$  estimates for a total of 112 of NGC 5128 star clusters, 89 of which are first-time measurements, in particular at faint absolute luminosities (see Section 4.1 and Figure 7). We find in our star cluster sample  $\mathcal{M}_{1/2}$  estimates ranging from the low-mass end,  $\mathcal{M}_{1/2,\text{min}} = 3.7_{-3.7}^{+8.9} \cdot 10^4 M_\odot$  (GC 0031), to the highest-mass object, GC 0365, with  $\mathcal{M}_{1/2,\text{max}} = 7.41_{-0.63}^{+0.51} \cdot 10^6 M_\odot$ , with a sample median  $\mathcal{M}_{1/2}$  of  $3.47 \cdot 10^5 M_\odot$ . By assuming that mass follows light, these masses translate into total mass estimates of  $\mathcal{M}_{\text{tot},\text{min}} = 7.4_{-7.4}^{+12.6} \cdot 10^4 M_\odot$  representative of the lower range of GC masses,  $\mathcal{M}_{\text{tot},\text{max}} = 1.48_{-0.89}^{+0.72} \cdot 10^7 M_\odot$  consistent with UCD masses, and a median  $\mathcal{M}_{\text{tot}} = 6.94 \cdot 10^5 M_\odot$ .

Alternatively, we use  $\sigma_0$  to estimate  $\mathcal{M}_{\text{dyn}}$  via Equation 2. By doing this, we lose the benefit of isotropy independence, but gain freedom from the underlying assumption that mass follows light. Encouragingly, we find very similar masses using either estimator at the low-mass tail of the GC mass distribution, with  $\mathcal{M}_{\text{dyn},\text{min}} = 7.6_{-7.6}^{+17.7} \cdot 10^4 M_\odot$ , and at the highest mass with  $\mathcal{M}_{\text{dyn},\text{max}} = 1.53_{-0.15}^{+0.12} \cdot 10^7 M_\odot$  and a median  $\mathcal{M}_{\text{dyn}}$  of  $7.04 \cdot 10^5 M_\odot$ . Interestingly, for total masses higher than  $\sim 1.0 \cdot 10^6 M_\odot$  we find that the relative difference between the estimators becomes more significant for certain clusters.

Figure 5 shows the relative difference between the total dynamical masses derived using  $2 \cdot \mathcal{M}_{1/2}$  and  $\mathcal{M}_{\text{dyn}}$  as a function of  $\mathcal{M}_{\text{dyn}}$  for each GC in our sample.  $\mathcal{M}_{\text{dyn}}$  essentially predicts similar (within  $\sim 1 - 5\%$ ) masses for “normal” GCs, ( $\lesssim 10^6 M_\odot$ ; typical of Local Group GCs). Above this threshold the discrepancy between the two mass estimates becomes more pronounced for certain clusters, reaching up to  $\sim 18\%$  higher  $\mathcal{M}_{\text{dyn}}$ . Altogether, this comparison suggests that for typical GC masses, i.e. in the range  $\sim 10^5 - 10^6 M_\odot$ , where cluster masses are completely dominated by baryonic material,  $\mathcal{M}_{1/2}$  is the more robust measure of the total GC mass. Above this mass range, and outside of  $r_h$  any kinematical tracers arising from, e.g. non-equilibrium configurations or/and dark gravitating mass components, may introduce biases in the mass estimates.

We calculate the dynamical mass-to-light ratios evaluated within the half-light radius ( $\Upsilon_V^{1/2}$ ) by dividing  $2 \cdot \mathcal{M}_{1/2}$  by the

TABLE 2  
STAR CLUSTER KINEMATICS

ID	$R_{gc}$	$v_{r,lit}$	$v_{r,ppxf}$	$\sigma_{ppxf}$	$\sigma_{m,ap}$	$\sigma_{m,gl}$	$\sigma_0$	$\sigma_{1/2}$	Ref.
(1)	[arcmin]	[km s <sup>-1</sup> ]	[km s <sup>-1</sup> ]	[km s <sup>-1</sup> ]	[km s <sup>-1</sup> ]	(10)			
GC 0028	11.30	558±97	512±1.80	8.95±2.10	8.97 <sup>+2.06</sup> <sub>-2.11</sub>	8.60 <sup>+1.80</sup> <sub>-1.92</sub>	9.87 <sup>+2.26</sup> <sub>-2.25</sub>	9.52 <sup>+2.27</sup> <sub>-2.25</sub>	1
GC 0031	10.63	595±202	552±2.80	3.69±4.35	3.67 <sup>+4.34</sup> <sub>-3.65</sub>	3.54 <sup>+4.05</sup> <sub>-3.53</sub>	4.12 <sup>+4.77</sup> <sub>-4.11</sub>	3.94 <sup>+4.68</sup> <sub>-3.93</sub>	1
GC 0048	11.36	509±15	481±1.10	7.61±1.40	7.62 <sup>+1.38</sup> <sub>-1.38</sub>	7.08 <sup>+1.13</sup> <sub>-1.18</sub>	8.25 <sup>+1.54</sup> <sub>-1.52</sub>	7.93 <sup>+1.48</sup> <sub>-1.45</sub>	1
GC 0050	8.03	718±16	732±0.70	10.09±0.90	10.01 <sup>+0.98</sup> <sub>-0.82</sub>	9.01 <sup>+0.71</sup> <sub>-0.61</sub>	10.65 <sup>+0.82</sup> <sub>-0.96</sub>	10.08 <sup>+0.92</sup> <sub>-0.84</sub>	1
GC 0052	7.89	276±59	199±15.25	1.09±51.85	...	...	...	...	2
GC 0053	7.75	503±17	505±1.00	10.50±1.20	10.55 <sup>+1.10</sup> <sub>-1.28</sub>	9.95 <sup>+0.83</sup> <sub>-1.03</sub>	11.91 <sup>+1.25</sup> <sub>-1.42</sub>	11.31 <sup>+1.29</sup> <sub>-1.41</sub>	1
GC 0054	8.12	736±58	734±1.50	9.31±1.70	9.30 <sup>+1.72</sup> <sub>-1.68</sub>	8.16 <sup>+1.36</sup> <sub>-1.38</sub>	9.60 <sup>+1.84</sup> <sub>-1.83</sub>	9.23 <sup>+1.63</sup> <sub>-1.75</sub>	3
GC 0058	8.06	685±43	684±0.80	7.60±1.10	7.61 <sup>+1.06</sup> <sub>-1.11</sub>	7.47 <sup>+0.92</sup> <sub>-1.03</sub>	8.50 <sup>+1.32</sup> <sub>-1.22</sub>	8.24 <sup>+1.23</sup> <sub>-1.31</sub>	2
GC 0064	9.42	594±36	574±2.90	16.29±2.90	16.27 <sup>+2.89</sup> <sub>-2.89</sub>	15.29 <sup>+2.40</sup> <sub>-2.50</sub>	17.79 <sup>+3.35</sup> <sub>-2.95</sub>	17.08 <sup>+3.14</sup> <sub>-3.06</sub>	1
GC 0065	6.92	331±47	278±1.30	9.78±1.62	9.78 <sup>+1.58</sup> <sub>-1.64</sub>	9.13 <sup>+1.26</sup> <sub>-1.37</sub>	11.25 <sup>+1.76</sup> <sub>-1.96</sub>	10.55 <sup>+1.71</sup> <sub>-1.78</sub>	2

NOTE. — Kinematical data for the NGC 5128 star clusters. Cols. 1 and 2 list the cluster IDs and projected galacto-centric radii respectively, cols. 3 and 4 list radial velocities, and cols. 5-9 list  $\sigma$  measured with *ppxf* and values which have been aperture-corrected to various cluster radii (see § 3.5 for details). Where available, all  $v_{r,lit}$  values are taken from Woodley et al. (2010a) corresponding to their “mean” values otherwise we adopt the best matches from either Woodley et al. (2007) or the estimates from Woodley et al. (2010a) that are based on individual spectra. Table 2 is published in its entirety in the electronic edition of the *Astrophysical Journal*. A portion is shown here for guidance regarding its form and content. References for  $v_{r,lit}$ : (1) Woodley et al. (2010a); (2) Woodley et al. (2007), their mean; (3) Woodley et al. (2007), LDSS2; (4) Woodley et al. (2007), VIMOS; (5) Woodley et al. (2007), Hydra.

TABLE 3  
STAR CLUSTER STRUCTURAL PARAMETERS

ID	$\mathcal{M}_{1/2}$	$\mathcal{M}_{dyn}$	$\Upsilon_{1/2}$	$\Upsilon_{dyn}$	$r_h$	$c$	Ref.
(1)	[ $M_\odot$ ]	[ $M_\odot$ ]	[ $M_\odot/L_\odot$ ]	[ $M_\odot/L_\odot$ ]	[pc]	(7)	(8)
GC0028	0.25 <sup>+0.12</sup> <sub>-0.12</sub>	0.50 <sup>+0.24</sup> <sub>-0.24</sub>	3.42 <sup>+1.71</sup> <sub>-1.70</sub>	3.45 <sup>+1.66</sup> <sub>-1.66</sub>	2.96±0.43	1.48	1
GC0031	0.04 <sup>+0.09</sup> <sub>-0.04</sub>	0.08 <sup>+0.18</sup> <sub>-0.08</sub>	0.49 <sup>+1.16</sup> <sub>-0.48</sub>	0.50 <sup>+1.16</sup> <sub>-0.49</sub>	2.58±0.43	1.48	1
GC0048	0.24 <sup>+0.09</sup> <sub>-0.09</sub>	0.48 <sup>+0.19</sup> <sub>-0.19</sub>	2.50 <sup>+0.98</sup> <sub>-0.96</sub>	2.54 <sup>+0.99</sup> <sub>-0.98</sub>	4.08±0.43	1.65	2
GC0050	0.66 <sup>+0.13</sup> <sub>-0.12</sub>	1.39 <sup>+0.23</sup> <sub>-0.26</sub>	3.43 <sup>+0.68</sup> <sub>-0.63</sub>	3.59 <sup>+0.62</sup> <sub>-0.70</sub>	7.03±0.43	1.56	2
GC0052	...	...	...	...	1.02±0.43	1.48	1
GC0053	0.33 <sup>+0.09</sup> <sub>-0.10</sub>	0.68 <sup>+0.18</sup> <sub>-0.19</sub>	3.61 <sup>+1.02</sup> <sub>-1.08</sub>	3.76 <sup>+1.00</sup> <sub>-1.09</sub>	2.74±0.43	1.83	2
GC0054	0.71 <sup>+0.25</sup> <sub>-0.27</sub>	1.45 <sup>+0.56</sup> <sub>-0.56</sub>	4.04 <sup>+1.45</sup> <sub>-1.56</sub>	4.10 <sup>+1.59</sup> <sub>-1.59</sub>	9.01±0.43	1.65	2
GC0058	0.12 <sup>+0.05</sup> <sub>-0.05</sub>	0.24 <sup>+0.09</sup> <sub>-0.09</sub>	1.14 <sup>+0.43</sup> <sub>-0.45</sub>	1.14 <sup>+0.44</sup> <sub>-0.42</sub>	1.89±0.43	1.43	1
GC0064	1.02 <sup>+0.39</sup> <sub>-0.39</sub>	2.08 <sup>+0.82</sup> <sub>-0.73</sub>	18.65 <sup>+7.24</sup> <sub>-7.07</sub>	18.97 <sup>+7.52</sup> <sub>-6.72</sub>	3.77±0.43	1.57	1
GC0065	0.28 <sup>+0.10</sup> <sub>-0.11</sub>	0.60 <sup>+0.21</sup> <sub>-0.23</sub>	2.23 <sup>+0.81</sup> <sub>-0.84</sub>	2.38 <sup>+0.84</sup> <sub>-0.92</sub>	2.71±0.43	1.99	1

NOTE. — Structural parameters and dynamical masses of our GC sample. GC0082, GC0107, GC0214, GC0219, GC0236, GC0262, GC0274, GC0417, GC0418, GC0420, GC0439, GC0435, and GC0437 are based on de-reddened  $r'$  band data. Table 3 is published in its entirety in the electronic edition of the *Astrophysical Journal*. A portion is shown here for guidance regarding its form and content. References for  $r_h$  and  $c$ : (1) Gomez et al. (2015, *in prep.*); (2) Jordán et al. (2015, *in prep.*); (3) Harris et al. (2002a).

total, de-reddened  $V$ -band luminosity, calculated as,

$$L_V = 10^{-0.4(V_0 - (m-M)_0 - M_{V,\odot})} \quad (4)$$

where  $M_{V,\odot} = 4.83$  mag. We also calculate dynamical mass-to-light ratios based on  $\sigma_0$  ( $\Upsilon_V^{dyn}$ ) by dividing  $\mathcal{M}_{dyn}$  by  $L_V$ . Most of our sample have apparent  $V$ -band magnitudes provided in the Woodley et al. (2007) catalogue (see also references therein), for which we list the de-reddened values in Table 1. We account for foreground reddening on an individual basis, with no attempt to correct for extinction internal to NGC 5128, by using the *Galactic Extinction and Reddening Calculator*<sup>10</sup> with the galactic reddening maps of Schlafly & Finkbeiner (2011). Where  $V$ -band magnitudes are not available, we list de-reddened  $r'$ -band magnitudes from Sinnott et al. (2010). If no photometry in the previously mentioned

filters is available, we base our  $\Upsilon_V$  estimates on the  $R$ -band magnitudes from the acquisition images, assuming in all cases a conservative photometric error of 0.1 mag.

We find a large spread in the corresponding  $\Upsilon_V^{1/2}$  ranging between  $0.49 M_\odot L_{V,\odot}^{-1}$  for GC 0031 up to  $64.47 M_\odot L_{V,\odot}^{-1}$  for GC 0225, with a sample median  $\Upsilon_V^{1/2}$  of  $3.33 M_\odot L_{V,\odot}^{-1}$ . Similarly, we find  $0.50 \leq \Upsilon_V^{dyn} \leq 66.61 M_\odot L_{V,\odot}^{-1}$  with a slightly higher median value of  $3.44 M_\odot L_{V,\odot}^{-1}$ . While these results are smaller by 0.47 and 0.36  $M_\odot L_{V,\odot}^{-1}$  than the median of  $3.8 M_\odot L_{V,\odot}^{-1}$  found by Taylor et al. (2010) for NGC 5128 GCs, they are notably higher than the median  $\Upsilon_{V,dyn}$  of  $2.2 \pm 0.3$  for Milky Way (MW) GCs (McLaughlin 2000; McLaughlin & Fall 2008) and  $\Upsilon_{V,dyn} = 1.37 \pm 0.28$  for M31 GCs (Strader et al. 2011). This result should perhaps not be too surprising as our sample is biased toward GCs at

<sup>10</sup> <http://ned.ipac.caltech.edu/forms/calculator.html>

the bright end of the GC luminosity function (GCLF). Thus, we are most likely not including many GCs with typical Local Group GC masses so that our sample is biased to GCs above the  $\sim 2 \cdot 10^6 M_\odot$  threshold where  $\Upsilon_V^{\text{dyn}}$  begins to rise dramatically (e.g. Hasegan et al. 2005; Kissler-Patig et al. 2006; Mieske et al. 2006, 2008a; Taylor et al. 2010). Conversely, our sample includes not only those of Taylor et al., but many fainter GCs, thus reaching well below the aforementioned threshold and biasing our medians toward slightly lower values compared to previous studies.

#### 4. DISCUSSION

Correlations between  $\Upsilon_V^{\text{dyn}}$ ,  $\mathcal{M}_{\text{dyn}}$ , and absolute magnitude ( $M_V$ ) can provide important information on the dynamic configuration and baryonic makeup of star clusters. To investigate these relations,  $\Upsilon_V^{\text{dyn}}$  is shown as a function of  $\mathcal{M}_{\text{dyn}}$  and  $M_V$  for each of our sample GCs in Figures 6 and 7 respectively, with the color shading parametrizing GC  $r_h$ .

Given that the following discussion hinges strongly on the features seen in Figures 6 and 7 having astrophysical explanations, we first considered several systematic effects and performed corresponding tests to check whether these could bias our measurements and artificially generate the observed results. The description of these tests, including detailed checks for data analysis biases, target confusion, correlations with galactocentric radius ( $R_{\text{gc}}$ ), and/or insufficient background light subtraction is provided in the Appendix. In summary, none of the tested effects are likely to explain the observed features in Figure 6 and 7, and thus we consider astrophysical explanations in what follows.

##### 4.1. $\mathcal{M}_{\text{dyn}}$ vs. $\Upsilon_V^{\text{dyn}}$ Relations

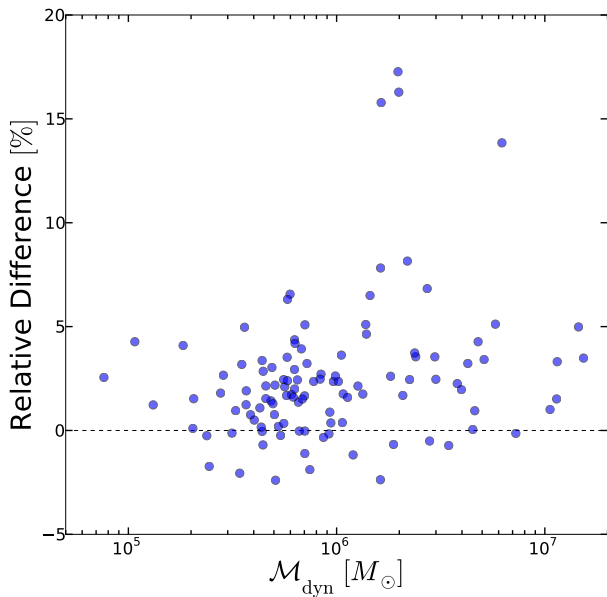


FIG. 5.— Relative difference between the traditionally used dynamical mass  $\mathcal{M}_{\text{dyn}}$  and twice the half-mass, i.e.  $\mathcal{M}_{\text{dyn}} - 2 \cdot \mathcal{M}_{1/2}$ , as a function of dynamical mass,  $\mathcal{M}_{\text{dyn}}$ . If mass follows light, then the total GC mass should be approximated by twice  $\mathcal{M}_{1/2}$ , hence, the difference being close to zero (dashed line). Here,  $\mathcal{M}_{\text{dyn}}$  predicts somewhat higher masses than  $2 \cdot \mathcal{M}_{1/2}$  for GCs with  $\mathcal{M}_{\text{dyn}} \gtrsim 10^6 M_\odot$ , indicating that for these clusters, mass may not strictly follow light and either dark gravitating mass components or non-equilibrium configurations may become necessary to explain the discrepancy in dynamical mass estimates of these clusters.

A number of interesting features shown by Figure 6 regarding the mass, size and mass-to-light ratios of our sample GCs are of note. We see a clear bifurcation in the  $\Upsilon_V^{\text{dyn}} - \mathcal{M}_{\text{dyn}}$  relations at  $\mathcal{M}_{\text{dyn}} \gtrsim 10^6 M_\odot$ , with two well defined sequences of GCs showing distinct positive slopes. GCs below  $\mathcal{M}_{\text{dyn}} \approx 10^6 M_\odot$  do not seem to follow either of these two relations, appearing to have mass-to-light ratios in the range of  $\sim 1-5$  with no particularly well defined correlation. In general, the circular points in Figures 6 and 7 indicate a smooth transition from GCs with masses  $\mathcal{M}_{\text{dyn}} \approx 10^5 - 10^6 M_\odot$  to those with  $\gtrsim 10^6 M_\odot$  that follow the two sequences.

To compare our measurements with similar data of Local Group GCs we overplot measurements from McLaughlin & van der Marel (2005) for Milky Way (MW), Large Magellanic Cloud (LMC), and Small Magellanic Cloud (SMC) GCs, along with data taken from Strader et al. (2011) for M31 GCs. It is important to point out here that while the Strader et al. measurements are based on direct kinematical measurements, the same cannot be said for the McLaughlin & van der Marel (2005) data since they are based  $\sigma_0$  estimates extrapolated from modelled light profiles. Thus, while we use the McLaughlin & van der Marel data as a large, homogeneous comparison dataset, a true comparison cannot be made until  $\mathcal{M}_{\text{dyn}}$  measurements can be made for a large sample of MW GCs based directly on stellar kinematics. With that said, both samples align well with the bulk of our NGC 5128 GC sample but extend to significantly lower masses and fainter luminosities. From the comparison with the majority of the Local Group GC sample, we conclude that the NGC 5128 GC sub-sample with  $\mathcal{M}_{\text{dyn}} \lesssim 10^6 M_\odot$  and  $\Upsilon_V^{\text{dyn}} \lesssim 5 M_\odot L_\odot^{-1}$  can be regarded as “classical” GCs similar to those found in the Local Group that follow the well-known GC “fundamental plane” relations (Djorgovski 1995; McLaughlin 2000) where non-core-collapse GCs in the MW show almost constant core mass-to-light ratios of  $\Upsilon_{V,0} = 1.45 M_\odot L_\odot^{-1}$ .

It is difficult to establish whether the fundamental plane relations strictly hold for the “classical” NGC 5128 sub-sample as the core surface brightness values of these clusters are not accessible, even with *HST* imaging. Even so, it can be seen in the middle panel of Figure 8, which compares the mass/light properties of our NGC 5128 sample with the Local Group GCs that the three distributions show a very similar rise up to  $\Upsilon_V^{\text{dyn}} \approx 2 M_\odot L_\odot^{-1}$ ; above which the NGC 5128 sample dominates. With a MW/SMC/LMC sample that underrepresents the peak of the GCLF at  $L_{V,0} \approx 2 \cdot 10^5 L_\odot$  (see bottom panel of Figure 8), it is beyond the scope of this work to verify whether a larger sample of MW/SMC/LMC GCs would “fill in” the distribution shown by our NGC 5128 sample. The M31 sample, on the other hand, tends toward lower  $\mathcal{M}_{\text{dyn}}$ , despite sampling a similar luminosity range as our NGC 5128 data. We thus, for now, consider the NGC 5128 GC sub-sample shown by the circular points in Figures 6 and 7 to simply represent the GCs that populate the Local Group.

More generally, we note that most NGC 5128 GCs have  $\Upsilon_V^{\text{dyn}}$  greater than the median value of MW/SMC/LMC GCs ( $\Upsilon_{\text{MW}}^{\text{dyn}} \approx 2.2 M_\odot L_\odot^{-1}$ ) and significantly higher values than for M31 GCs ( $\Upsilon_{\text{M31}}^{\text{dyn}} \approx 1.37 M_\odot L_\odot^{-1}$ ), although the latter may be due to insufficient aperture corrections for extended GCs (see discussion in Strader et al. 2011). With a median  $\Upsilon_V^{\text{dyn}}$  of  $3.44 M_\odot L_\odot^{-1}$ , it is tempting to suggest a fundamental difference between Local Group GCs and those in NGC 5128. We

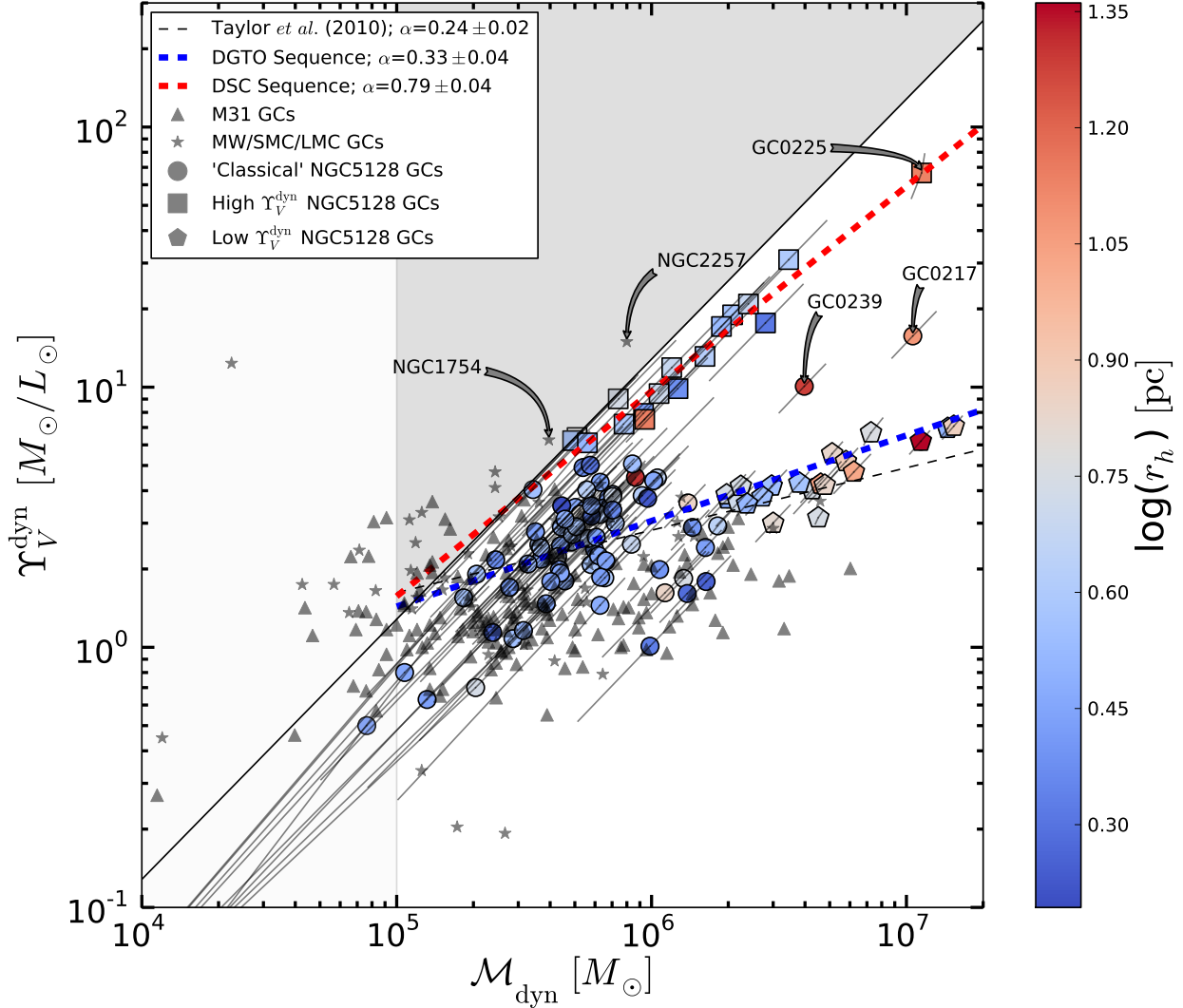


FIG. 6.—  $\Upsilon_V^{\text{dyn}}$  as a function of  $\mathcal{M}_{\text{dyn}}$ , with the color shading indicating the half-light radius of the clusters. Three groups of GCs corresponding to “classical” GCs, and to the “low-” and “DSC” sequence GCs are indicated by circular, pentagonal, and square symbols, respectively (see legend). The empirical power-law relation of Taylor et al. (2010) is shown by the thin dashed black line, while steeper power-law fits based on the two  $\Upsilon_V^{\text{dyn}}$  branches are shown by the colored thick dashed lines. The steepest relation (red) is based only on the square points which have been isolated based on their faint absolute magnitudes ( $M_V \gtrsim -8.5$  mag) and high mass-to-light ratios ( $\Upsilon_V^{\text{dyn}} \geq 6.0 M_\odot L_{V,\odot}^{-1}$ ). Meanwhile, the blue dashed line shows the results of fitting only the pentagonal points with  $\Upsilon_V^{\text{dyn}} \leq 10.0 M_\odot L_{V,\odot}^{-1}$  and  $\mathcal{M}_{\text{dyn}} \geq 2 \cdot 10^6 M_\odot$ . The solid black line and dark gray shading illustrate the observational limit to our data, while the light gray shading indicates an approximate lower mass limit for selected GCs in our spectroscopic sample. Several interesting objects that are discussed in the text are labeled with their catalog numbers. We plot corresponding measurements for Local Group GCs as grey stars (MW/SMC/LMC; taken from McLaughlin & van der Marel 2005) and grey triangles (M31; taken from Strader et al. 2011).

do not strictly support this notion, as a more straight-forward interpretation is that we are simply sampling part of the GCMF that is inaccessible in the Local Group due to a dearth of known GCs above  $10^6 M_\odot$ . Indeed, the top panel of Figure 8 demonstrates that the  $\mathcal{M}_{\text{dyn}}$  distributions of the Local Group and NGC 5128 GC samples are very dissimilar; the highest values are reached by NGC 5128 GCs, followed by M31 and the MW/SMC/LMC. Above  $\mathcal{M}_{\text{dyn}} \approx 5 \cdot 10^5 M_\odot$ , the NGC 5128 sample is well represented up to  $\sim 10^7 M_\odot$ , while Local Group GCs are more populous toward the lower tail of the GCMF. Altogether, Figure 8 suggests that the NGC 5128/Local Group GCSs may have fundamentally dif-

ferent GCMFs, given the similarly sampled GCLF (bottom panel), something that can be tested when similar NGC 5128 data probing fainter magnitudes becomes available.

Having addressed the main, “classical” body of GCs in Figure 6, we now turn to the two distinct high- $\mathcal{M}_{\text{dyn}}$  sequences. In the following we refer to GCs with  $\Upsilon_V^{\text{dyn}} \gtrsim 6$  and luminosities fainter than  $M_V = -8.5$  mag (see Figure 7) as members of the “dark star cluster” (DSC) sequence (red dashed line in Figure 6) due to their potential connection to DSCs predicted by theory (see §4.3.2; Banerjee & Kroupa 2011). Those with  $\mathcal{M}_{\text{dyn}} \gtrsim 2 \cdot 10^6 M_\odot$  and  $\Upsilon_V^{\text{dyn}} \lesssim 10$  that follow the shallower  $\Upsilon_V^{\text{dyn}} - \mathcal{M}_{\text{dyn}}$  relation (blue dashed line in Figure 6), we

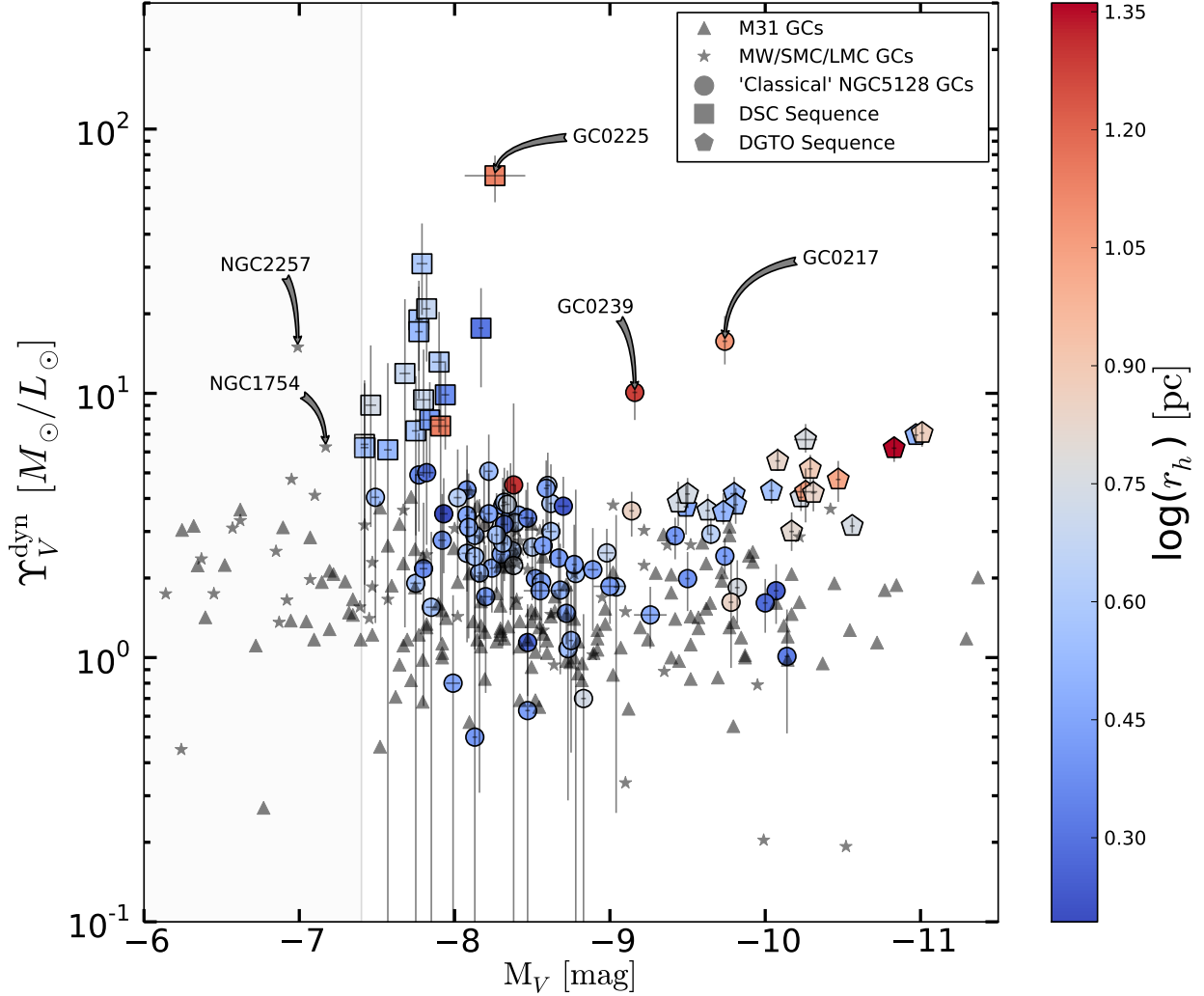


FIG. 7. —  $\Upsilon_V^{\text{dyn}}$  as a function of  $M_V$ , with cluster half-light radius indicated by the color bar. Symbols are the same as in Fig. 6, with the same objects indicated. The vertical light-grey line and the shaded zone ( $M_V \geq -7.4$  mag) indicate the photometric limit of our spectroscopic sample selection.

refer to as members of the “dwarf-globular transition object” (DGTO) branch, since these objects encroach upon the structural parameter space of the DGTOs reported by Haşegan et al. (2005).

Interestingly, the two objects omitted by these criteria, GC0217 and GC0239, lie intermediate between these two sequences and so we refer to them as “intermediate- $\Upsilon_V^{\text{dyn}}$ ” star clusters (see Figure 6). Their properties may indicate either an evolutionary connection to one of the sequences, or perhaps represent a separate population that is simply not well sampled by our data. In terms of structural parameters, the mean  $r_h$  of the DSC sequence ( $\langle r_h \rangle_{\text{high}} = 5.10$  pc) is marginally smaller than that of the DGTO branch ( $\langle r_h \rangle_{\text{low}} = 6.67$  pc), while also smaller in the median (4.01 and 5.59 pc, respectively). Meanwhile, the mean galactocentric radii of the two populations are  $\langle R_{\text{gc}} \rangle_{\text{high}} = 6.97'$  and  $\langle R_{\text{gc}} \rangle_{\text{low}} = 9.11'$ . WELCH 2-sample tests yield that the mean differences in  $r_h$  and  $R_{\text{gc}}$  are not statistically significant, with p-values of 0.27 and 0.15, respectively.

#### 4.2. Properties of the $\Upsilon_V^{\text{dyn}}-\mathcal{M}_{\text{dyn}}$ Sequences

To probe the properties of the two  $\Upsilon_V^{\text{dyn}}-\mathcal{M}_{\text{dyn}}$  sequences, we fit empirical power-law relations of the form,

$$\Upsilon_V^{\text{dyn}} \propto \mathcal{M}_{\text{dyn}}^\alpha \quad (5)$$

to approximate the data. In a similar analysis of dispersion supported CSSs, including a subsample of the GCs considered here, Taylor et al. (2010) found a value of  $\alpha = 0.24 \pm 0.02$  to fit their data, connecting “classical” GCs to more massive systems like UCDs and dwarf elliptical galaxies. This relation is shown in Figure 6 by the thin dashed black line and is too shallow to fit either of the  $\Upsilon_V^{\text{dyn}}-\mathcal{M}_{\text{dyn}}$  sequences of the present GC sample. To better represent the data, we instead make an effort to fit power-laws to the sequences individually and find that each is well approximated by distinct, tight relations as described in the following.

The dashed blue line in Figure 6 shows an approximation to the DGTO sequence with a power-law slope of  $\alpha = 0.33 \pm 0.04$

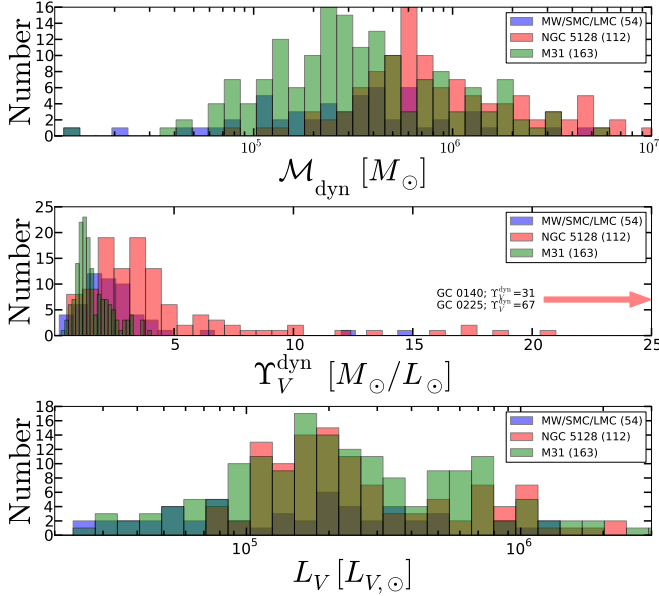


FIG. 8.— Comparison between the  $\mathcal{M}_{\text{dyn}}$  (top panel),  $\Upsilon_V^{\text{dyn}}$  (middle panel), and  $L_V$  (bottom panel) distributions for the NGC 5128 objects of the present work (red histograms), and Local Group GCs (MW/SMC/LMC; blue histograms), and M31; (green histograms)). Opacity has been lowered to show where the distributions overlap. While the MW/SMC/LMC sample is too small to make strong comparisons to the other two distributions, it is clear that the NGC 5128 sample shows higher median  $\mathcal{M}_{\text{dyn}}$  and  $\Upsilon_V^{\text{dyn}}$  than the M31 sample, despite probing a similar range in  $L_V$ . The total sample sizes are indicated in parentheses in the legends.

(pentagons in all relevant Figures). This relation fits the data quite well from the high mass GCs down to  $\sim 10^5 M_\odot$ , which represents a value more typical of Local Group GCs. Meanwhile, the DSC sequence (square points in all relevant Figures), shown by the red dashed line in Figure 6 with a steeper slope ( $\alpha = 0.79 \pm 0.04$ ), seems to be created by a fundamentally different collection of objects. Interestingly, we find two LMC GCs (NGC 2257 and NGC 1754, see Figure 6) that appear to align well with the DSC sequence. While no strong statements can be made about only two objects, their exclusive presence around a currently interacting satellite of the MW marks an interesting starting point to investigate any connection to the DSC sequence.

$\Upsilon_V^{\text{dyn}}$  is plotted as a function of  $M_V$  in Figure 7, which shows that the DGTO sequence is composed exclusively of the brightest GCs of the sample. Thus, the DGTO sequence may simply be explained by these GCs representing the high-luminosity tail of the GCLF. On the other hand, GCs on the DSC sequence are fainter than DGTO GCs by  $\Delta M_V \approx 1$  mag, making them similar in luminosity to the average GCLF turnover magnitude found in many GC systems. Furthermore, it can be seen that the range of  $r_h$  for the objects on the DSC sequence is not dramatically different from that of the “classical” or DGTO GCs. Collectively, the similarity shown by these DSC objects in luminosity and size to other GCs in many GCSs likely explains why they have not been identified before in other galaxies, as they are only remarkable in their stellar dynamics properties. Regardless, as this is the first time a clear distinction between two such groups of CSSs has been made, this naturally leads to the question of whether these objects should be called GCs at all.

### 4.3. Possible Origins of the $\Upsilon_V^{\text{dyn}}-\mathcal{M}_{\text{dyn}}$ Sequences

Having shown artificial biases to be unlikely drivers of our results (see Appendix), the following discusses several astrophysical mechanisms that may generate our observations.

If the DGTO sequence is made up of the brightest “classical” GCs, the  $\Upsilon_V^{\text{dyn}} \simeq 5-9$  values shown by some are still perplexing in that GCs with  $\Upsilon_V^{\text{dyn}} \gtrsim 5$  require additional explanations beyond being the extension of the “classical” GCLF. Effects that can mimic higher than usual  $\Upsilon_V^{\text{dyn}}$  include non-equilibrium dynamical processes (e.g. rotation, pre-relaxation, young stellar populations, tidal disruption) or an exotic IMF. We find several DGTO sequence GCs with ellipticities,  $\epsilon \gtrsim 0.25$ , indicative of a non-equilibrium dynamical state, such as rotation. Other GCs show young ( $\lesssim 8$  Gyr) ages (Woodley et al. 2010b), and thus may not be fully relaxed. Additionally, for four objects on this DGTO sequence (GC 0041, GC 0330, GC 0365, and GC 0378) Harris et al. (2002a) found evidence for extra-tidal light contributing to their surface-brightness profiles in excess of their King model fits. For the remainder, the possibility of a particularly bottom-heavy IMF (e.g. Dabringhausen et al. 2008; Mieske et al. 2008b) could explain their elevated  $\Upsilon_V^{\text{dyn}}$  estimates.

#### 4.3.1. Globular Cluster Rotation

To probe how non-equilibrium states could explain the elevated  $\Upsilon_V^{\text{dyn}}$ , we investigate the possible impact of rotation on our mass estimates. Treating the observed  $\Upsilon_V^{\text{dyn}}$  as being strictly the result of the GCs exhibiting a mass excess at a given luminosity with respect to the median  $\Upsilon_{\text{MW}}^{\text{dyn}} = 2.2$ , we calculate for each of our sample GCs the amount of “extra” mass within  $r_h$ , or  $\Delta \mathcal{M}_{1/2} = (\Upsilon_V^{\text{dyn}} - \Upsilon_{\text{MW}}^{\text{dyn}}) \cdot \frac{L_V}{2} = (\Upsilon_V^{\text{dyn}} - 2.2) \cdot \frac{L_V}{2}$ . This mass component then needs to be accounted for by the effects discussed above to explain the elevated  $\Upsilon_V^{\text{dyn}}$  values.

Making the naive assumption that  $\Delta \mathcal{M}_{1/2}$  is entirely due to rotation, then in the general situation where the rotation axis is aligned at any angle  $i$  with respect to the observational plane, stars at  $r_h$  would require circular velocities of at least,

$$v \sin i \simeq \left( \frac{\Delta \mathcal{M}_{1/2} G}{r_h} \right)^{1/2}. \quad (6)$$

To investigate how rotation could explain the  $\Upsilon_V^{\text{dyn}}$  estimates, the left panel of Figure 9 shows a comparison between  $v \sin i$  and the average stellar velocity in GCs computed from the random stellar motions via  $\sigma_{1/2} \sqrt{3}$ . The symbols are the same as in Figures 6 and 7, but with “classical” GCs simply shown as dots. The dashed line in Figure 9 indicates the boundary at which rotation is equal to the random stellar motion component required to be consistent with  $\Delta \mathcal{M}_{1/2}$ . It must be acknowledged that the errors bars shown on Figure 9 make it impossible to definitively discuss the dynamical configurations of our sample. On the other hand, the lack of comingling between the different groups suggests that the features seen are probably not solely due to systematic errors, thus they can still be used to make general statements about the populations as wholes, and we proceed with that in mind.

A GC that has a rotation to random motion component ratio,  $v \sin i / \sigma_{1/2} \sqrt{3} > 1$ , requires circular velocity speeds that would destabilize the system if only rotation is to explain its

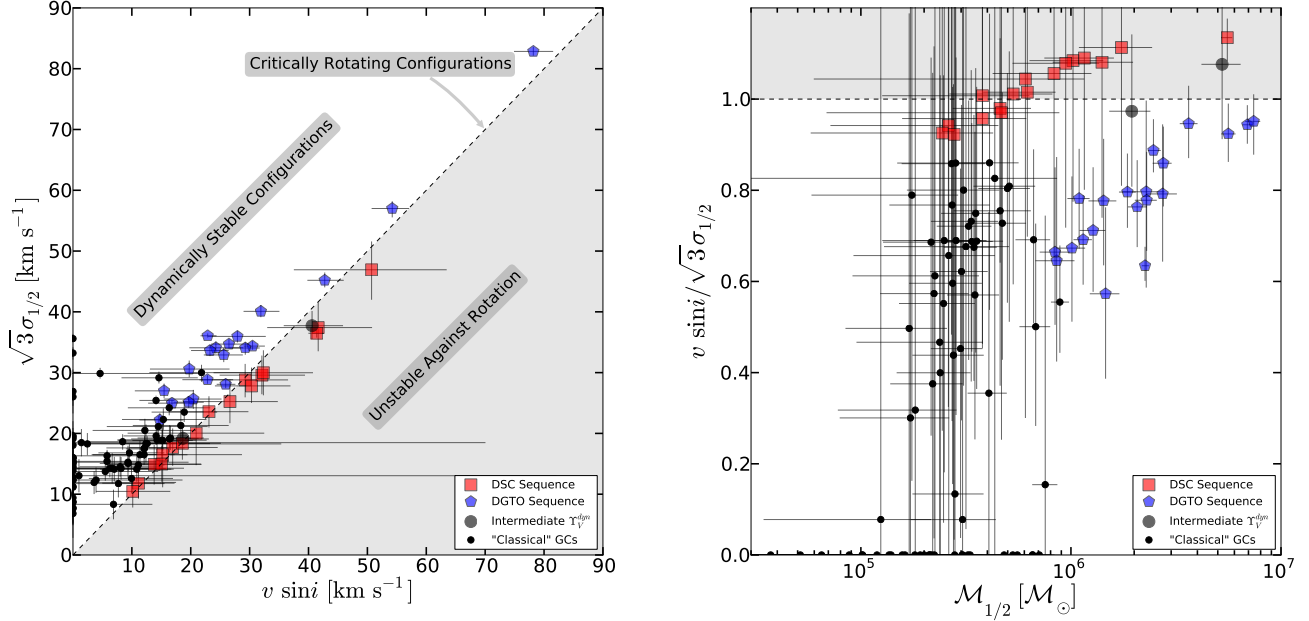


FIG. 9.— (Left panel): Average measured orbital velocities of cluster stars shown as a function of the minimum circular velocities necessary for rotation alone to account for the observed mass-to-light ratios. The dashed line represents the critical velocity (assuming  $\sin i = 1$ , or the maximum observable velocities) at which *a*) rotation alone is able to explain the elevated  $\Upsilon_V^{\text{dyn}}$  of an object, or/and *b*) an object of a given mass becomes unstable against rotation, consistent with a dynamical non-equilibrium state. Symbol shapes are as in Figures 6 and 7, but with the “classical” GCs shown as points and the two intermediate- $\Upsilon_V^{\text{dyn}}$  GCs (GC 0217 and GC 0239, see Section 4.1) shown as gray symbols. (Right panel):  $v \sin i / \sqrt{3}\sigma_{1/2}$  as a function of the dynamical half-mass,  $M_{1/2}$ , for the same objects. There are correlations for the objects on the DSC and DGTO sequences, with a weaker correlation shown by the “classical” GCs with  $v \sin i / \sqrt{3}\sigma_{1/2} \gtrsim 0.2$ , indicating that GCs become more rotationally supported at higher masses.

$\Delta M_{1/2}$ . Most DSC objects fall on or below this unity relation. These clusters are generally consistent with non-equilibrium dynamical configurations, and may require at least one other effect to explain their high  $\Upsilon_V^{\text{dyn}}$  values, e.g. dark gravitating components. On the other hand, a GC with  $v \sin i / \sigma_{1/2} \sqrt{3} < 1$  can have net angular momentum that can provide a stable configuration against rotational breakup. In this case, GC rotation alone can account for their  $\Upsilon_V^{\text{dyn}}$ . Significant error bars notwithstanding, all of the “classical” GCs along with those on the DGTO sequence are exclusively consistent with  $v \sin i / \sigma_{1/2} \sqrt{3} < 1$ . Thus, their elevated  $\Upsilon_V^{\text{dyn}}$  could be explained by rotation without the need to invoke additional components, bolstering the interpretation that they represent the high-luminosity tail of NGC 5128’s GCLF.

As a corollary of the previous exercise, we investigate in the right panel of Figure 9 whether the ratio  $v \sin i / \sigma_{1/2} \sqrt{3}$  correlates with  $M_{1/2}$  (see Section 3.6). We find that the DSC and DGTO GC samples appear to exhibit correlations in this parameter space, hinting at rotational support that increases with GC mass. This result concurs with the recent findings of Kacharov et al. (2014) and Fabricius et al. (2014), who measure small but significant rotational speeds in MW GCs. However, given that  $\sin i$  is likely to be randomly distributed in the range  $[0..1]$  (hence,  $\langle \sin i \rangle = 2/\pi$ ), these correlations, if real and due to rotational support alone, should be much noisier than what we see in the right panel of Figure 9, and are therefore probably driven by other effects than rotation alone.

#### 4.3.2. Central Massive Black Holes

A potential source of artificially enhanced  $M_{\text{dyn}}$  values are the effects of central intermediate-mass black holes (IMBHs; e.g. Safonova & Shastri 2010; Mieske et al. 2013; Leigh et al. 2014) of lesser mass, but otherwise not unlike that found recently in a UCD (Seth et al. 2014). To estimate the influence of a putative central compact object we compute expected IMBH masses by using our  $\sigma_0$  estimates with the BH mass vs. velocity dispersion relation,  $M_{\text{BH}} - \sigma$ , for CSSs, which is offset from that of pressure supported galactic systems (Mieske et al. 2013, their Figure 6). From the  $M_{\text{BH}} - \sigma$  relation, assuming that it scales to lower-mass stellar systems, we obtain BH masses in the following ranges  $6.6 \cdot 10^4 \lesssim M_{\text{BH}}/M_\odot \lesssim 5.0 \cdot 10^7$  for the DGTO GCs,  $8.5 \cdot 10^2 \lesssim M_{\text{BH}}/M_\odot \lesssim 2.2 \cdot 10^6$  for the DSC objects, and  $M_{\text{BH}} \lesssim 7.6 \cdot 10^5 M_\odot$  for the combined “classical” and intermediate- $\Upsilon_V^{\text{dyn}}$  sample.

For each GC we integrate the central stellar light profile using our numerical models (see §3.5) until the radius of the sphere encompasses a stellar mass corresponding to  $2M_{\text{BH}}$ , assuming the median  $\Upsilon_{\text{MW}}^{\text{dyn}} = 2.2$ . This radius defines the IMBH sphere of influence ( $r_i$ ; Merritt 2004). We then compute the fraction of the stars within this sphere with respect to the modeled population falling within our apertures,  $f(r < r_i)$ . In Figure 10, we plot this fraction as a function of  $M_{\text{dyn}}$  for our entire sample.

While most of the “classical” and intermediate- $\Upsilon_V^{\text{dyn}}$  GCs show little dynamical influence by potential IMBHs, there is an upturn in  $f(r < r_i)$  for GCs with  $M_{\text{dyn}} \gtrsim 10^6 M_\odot$ . The high-mass sub-sample is mostly made up of the DGTO and DSC objects. A MOOD test (Mood 1950) for equal medians (see horizontal lines in Figure 10) provides no evidence for

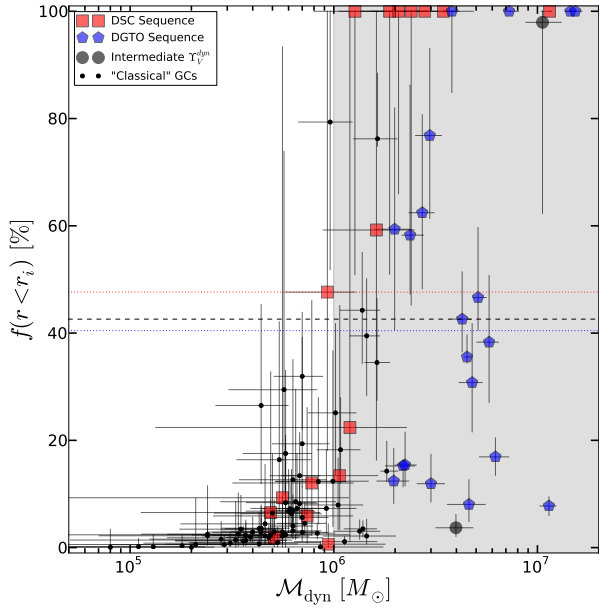


FIG. 10.— Fraction of the stellar mass within the sphere of influence of a putative central IMBH, as a function of  $\mathcal{M}_{\text{dyn}}$  for our entire sample. The black dashed line shows the median of the combined DGTO and DSC sequence GCs, while the red- and blue-dotted lines show the medians for the individual sub-samples.

a difference in the DGTO and DSC sequence  $f(r < r_i)$  ( $p$ -value=1.00). Specifically, Figure 10 shows a bimodal distribution in  $f(r < r_i)$  for the DSC sequence objects, as 7/17 and 8/17 fall either at the  $\sim 100\%$  or  $\lesssim 20\%$  levels, respectively. Two of these objects show intermediate  $f(r < r_i) \simeq 50 - 60\%$ . For the DGTO sequence GCs there is a smoother transition from those with little to no influence by a putative IMBH (7/20) to those which would have the majority of their stars dynamically dominated by such an object (8/20). Taken together, the presence of central IMBHs could in principle provide a plausible explanation for the observed dynamics of many objects on both sequences.

We point out that some GCs in the grey shaded region in Figure 10 are identified as X-ray sources, almost all of which are classified as Low-Mass X-ray Binary (LMXB) hosts from *Chandra* observations (Liu et al. 2011). 2/17 DSC objects are X-ray sources, compared to 8/20 DGTO GCs. This is in line with the following argument: given the fainter nature of the DSC objects, they must have fewer stars compared to DGTO clusters at a given  $\mathcal{M}_{\text{dyn}}$ . With fewer stars providing stellar winds/mass-loss, one would generally expect accretion onto an IMBH/LMXB to be less likely compared to DGTO sources.

Given the apparently enigmatic properties of the faint DSC subsample, it is important to note that BHs dominating their dynamics might alter our basic assumption of the canonically accepted King (1966) stellar density profile. Spatially resolved  $\sigma$  profiles would test the putative central BH sphere of influence and thus the validity of our assumption. Compared to a uniformly distributed mass component, a central IMBH can mimic a dynamical mass as much as  $4 - 5\times$  higher than the mass of the BH itself (Mieske et al. 2013). Scaling  $\Delta M_{1/2}$  in this sub-sample down by four then suggests that BHs of masses  $3.9 \cdot 10^4 \lesssim \mathcal{M}_{\text{BH}}/M_{\odot} \lesssim 1.3 \cdot 10^6$  could plausibly provide the  $\sigma_{\text{ppxf}}$  that we observe, as well as the elevated

$\Upsilon_V^{\text{dyn}}$  values. In any case, the lack of a strong correlation in the  $f(r < r_i)$  vs.  $\mathcal{M}_{\text{dyn}}$  plane calls into question whether IMBHs would be the only driver of the two sequences.

Despite the plausibility of single massive central BHs explaining some of our results, the potential connection to DSCs predicted recently by Banerjee & Kroupa (2011) needs to be considered. In this scenario, neutron star and BH remnants of massive stars gather as a very concentrated central dark sub-cluster. Passages through a strong tidal field act to strip luminous matter from the outskirts, resulting in very high mass-to-light ratios. To be observable, the stellar stripping process must act on timescales shorter than the self-depletion of dark remnants via encounter-driven mechanisms (e.g. three-body interactions). Banerjee & Kroupa (2011) predict lifetimes of such objects with stellar masses  $\lesssim 10^5 M_{\odot}$  orbiting within 5 kpc of a MW-like potential to be generally less than 1 Gyr, calling into question the likelihood of observing such a current population. With that said, we note that given our DSC stellar masses of  $\mathcal{M}_{*} \simeq 1 - 5 \cdot 10^5 M_{\odot}$ , and  $R_{\text{gc}} \gtrsim 5$  kpc, combined with the predicted correlation between lifetime, and both  $\mathcal{M}_{*}$  and  $R_{\text{gc}}$ , these clusters could plausibly have DSC phases lasting on Gyr timescales. Detailed future modeling will be critical in determining the plausible parameter space necessary for the existence of these objects given the unique history of NGC 5128.

#### 4.3.3. Dark Matter Halos

If central IMBHs are not driving the dynamics of the DSC sequence, then explaining objects with  $\Upsilon_V^{\text{dyn}} \gtrsim 10$  becomes very difficult without requiring a significant amount of dark matter (DM). It is generally accepted that “classical” GCs are devoid of non-baryonic matter, but this cannot be entirely ruled out (e.g. Moore 1996; Conroy et al. 2011; Sollima et al. 2012; Ibata et al. 2013) and may in fact be expected from theoretical considerations (e.g. Peebles 1984; Saitoh et al. 2006). Having considered and ruled out inflated  $\Upsilon_V^{\text{dyn}}$  values due to myriad observational/instrumental effects (see Appendix), and/or severely out-of-equilibrium dynamical states (see Section 4.3.1) due to, e.g., rotation, we now consider the implications of the DSC sequence being due to the onset of DM domination in low-mass systems ( $\mathcal{M} \gtrsim 10^5 M_{\odot}$ ).

The red-dashed line in Figure 11 shows the difference in  $\Upsilon_V^{\text{dyn}}$  between the DGTO and DSC power-law fits as a function of  $\mathcal{M}_{\text{dyn}}$ . In other words, this relation shows the amount of DM required to explain the exponentially increasing mass excess compared to “classical” GCs. If dark matter is behind the DSC objects, then the sharp truncation at  $\mathcal{M}_{\text{dyn}} \approx 10^5 M_{\odot}$  hints at a population of increasingly DM dominated structures in the immediate vicinity of NGC 5128 with masses as low as a few times  $10^5 M_{\odot}$ .

Recent modeling has shown that in a realistic galaxy cluster potential, as much as 80-90% of a dwarf galaxy’s DM halo may be stripped before baryonic losses become observable (Smith et al. 2013a). If the DSC objects originate from low-mass halos that have been stripped during their passage(s) through NGC 5128’s potential well, this then implies progenitors of  $\mathcal{M}_{\text{dyn}}$  (and thus  $\Upsilon_V^{\text{dyn}}$ )  $\sim 10\times$  higher than we observe. This scenario would suggest that at one point in time during the assembly history of NGC 5128 there may have been a population of compact, low-luminosity baryonic structures inside the virial radius of NGC 5128 embedded within extraordinarily compact dark matter halos of  $10^7 \lesssim \mathcal{M}_{\text{dyn}}/M_{\odot} \lesssim 10^8$  with  $100 \lesssim \Upsilon_V^{\text{dyn}}/M_{\odot} L_{\odot}^{-1} \lesssim 700$  (e.g.

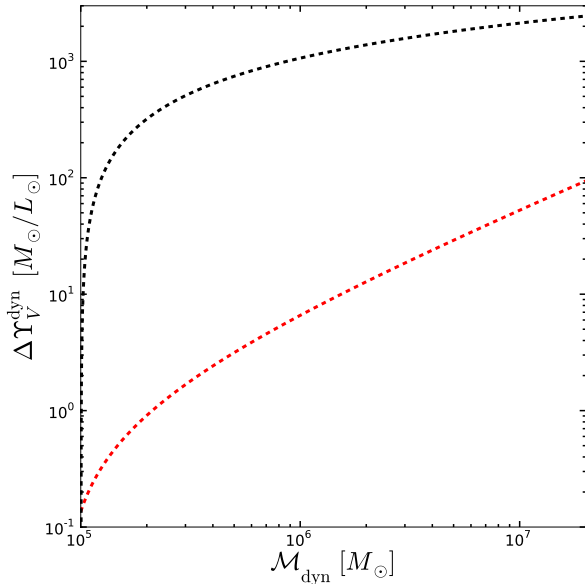


FIG. 11.— Difference in  $\Upsilon_V^{\text{dyn}}$  between the red- and blue-dashed lines in Figure 6 (red relation), and the observational limit of our data (black relation) as a function of  $\mathcal{M}_{\text{dyn}}$ . The dominance of the dark gravitating mass component exponentially increases above a truncation mass of a few times  $10^5 M_\odot$ .

Ricotti 2003).

If the above is true, then the truncation of the red-dashed line in Figure 11 at  $\sim 10^5 \mathcal{M}_{\text{dyn}}$  may mark the limit below which primordial DM halos have not survived accretion events onto larger galaxy structures. This result is consistent with the picture recently put forward in Puzia et al. (2014) where the sizes of outer halo star clusters are truncated by the abundance of small DM halos (see also Carlberg 2009; Carlberg et al. 2011; Carlberg & Grillmair 2013). In this scenario, CSSs of larger masses suffer higher levels of dynamical friction than low-mass clusters while moving through the potential well of the host galaxy and sink closer in to the central body (e.g. Lotz et al. 2001). While sinking, they suffer extra harassing encounters in the more crowded core region, which act to further truncate their sizes (e.g. Webb et al. 2013). The above may be the explanation for why the DSC objects have sizes typical of Milky Way GCs (see Figures 6 and 7, and also Figure 16 in Puzia et al. 2014).

#### 4.4. Potential Progenitors of the DSC Sequence GCs

Figure 7 shows that with magnitudes of  $-8.5 \lesssim M_V \lesssim -7.4$  mag, the DSC objects are among the intrinsically faintest star clusters of our sample. This range scratches the peak of the GCLF and begins to infringe upon the realm of ultra-faint dwarf galaxies (UFDs) in the Local Group, which are thought to be the extension of the dwarf spheroidal (dSph) galaxy population to lower luminosities ( $M_V \gtrsim -8$  mag; e.g., Willman et al. 2005; Zucker et al. 2006; Belokurov et al. 2007; Zucker et al. 2007; McConnachie et al. 2009; Brown et al. 2012). Despite smaller sizes than known Local Group dSphs, the combination of high  $\Upsilon_V^{\text{dyn}}$  and low luminosities shown may suggest an evolutionary link to a putative population of dSph- and/or UFD-like, dark-matter dominated dwarf galaxies. If so, they must have undergone an extremely compact and therefore efficient early star-formation burst before being

tidally stripped of most of their dark-matter halos during subsequent interactions with NGC 5128 (e.g. Smith et al. 2013a; Garrison-Kimmel et al. 2014; Sawala et al. 2014).

The fact that we do not observe current tidal features indicative of stripping might be due to the surface brightness limits of available data, but higher (i.e. non-equilibrium) LOSVDs might still be consistent with theoretical predictions. For instance, Smith et al. (2013b) model a dwarf galaxy similar to the UFD UMaII, which with  $\sigma = 6.7 \text{ km s}^{-1}$  (implying  $\Upsilon_V^{\text{dyn}} \approx 1000$ ; Simon & Geha 2007) is an obvious likely candidate for a DSC sequence object progenitor. By subjecting it to tidal forces in a Milky Way-like gravitational potential, these authors successfully reproduced many observed properties (e.g. luminosity, central surface brightness, ellipticity, etc.) of UMaII, and found that the galaxy’s  $\sigma$  can be boosted on timescales of a few Gyr, in particular around the apocentre of the orbit. Their modeling showed that “ $\sigma$  boosting” can easily reproduce UMaII’s  $\sigma$ , and can even reach extreme levels of  $> 20 \text{ km s}^{-1}$  when the orbital trajectory is close to being perpendicular to the disk of the host galaxy. The models therefore suggest that the extreme  $\Upsilon_V^{\text{dyn}}$  for the DSC objects could potentially be explained without requiring large amounts of DM. While this result, assuming that “ $\sigma$  boosting” scales to a gE galaxy like NGC 5128, might be sufficient to explain a handful of the DSC clusters, we consider it highly unlikely that all such clusters can be accounted for, due to the required synchronization of their apocentre passages and current line-of-sight alignments. Note that this mechanism would generally introduce scatter rather than producing the sequences observed in Figure 6.

Assuming that “ $\sigma$  boosting” is unable to solely account for the DSC objects, then the small sizes compared to UFD-like galaxies call for careful skepticism if DM is the preferred explanation. For example, characteristic central DM densities for dwarf galaxies, if canonical halo profiles are assumed, can range from  $0.1 M_\odot \text{ pc}^{-3}$  for preferred cored profiles, to as much as  $60 M_\odot \text{ pc}^{-3}$  for cuspy profiles (e.g. Gilmore et al. 2007; Tollerud et al. 2011). In this case, the required DM masses ( $\mathcal{M}_{\text{DM}}$ ) of  $1.6 \cdot 10^5 < \mathcal{M}_{\text{DM}}/M_\odot < 5.4 \cdot 10^6$  and corresponding densities ( $\rho_{\text{DM}}$ ) of  $40 < \rho_{\text{DM}}/M_\odot \text{ pc}^{-3} < 4.5 \cdot 10^4$  within the DSC cluster half-light radii are at least three orders of magnitude higher than those expected from a cuspy dwarf galaxy profile, or if cored, they would each need to be embedded in  $\sim 10^{14} - 10^{15} M_\odot$  halos.

Irrespective of this problem, such high DM densities might actually give rise to central baryonic concentrations that enable the formation of IMBHs. This might be realized by triggering an extremely dense central stellar environment, leading to a runaway collisional event that culminates with the formation of a central BH that might continue to grow through the accretion of binary star and higher-order multiples.

Given all of these interpretations, it seems just as likely that a combination of central IMBHs and/or dark stellar remnants, cuspiest-than-expected DM halos, and/or “ $\sigma$  boosting” could be at work. This conclusion may in fact be the most reasonable one, given that IMBHs would presumably be of dwarf galaxy origin given the difficulty in building up such a mass in a GC-like structure without just as remarkable early star-formation efficiency. Then, the residual DM leftover after stripping, if cuspy, in combination with “ $\sigma$  boosting”, may be sufficient to produce these new objects. This final interpretation would then require both less extreme BH and DM masses, while avoiding the orbital synchronization problem. Regard-

less of the mechanism giving rise to them, the emergence of the DSC sequence objects is a very unexpected result and calls for detailed follow-up observations and high spatial resolution modeling.

## 5. SUMMARY & FUTURE OUTLOOK

New high-resolution spectra of compact stellar objects around the giant elliptical galaxy NGC 5128 (Centaurus A) were analyzed. We combined these data with a re-analysis of 23 clusters from the literature and used a penalized pixel fitting technique to derive new radial velocities for 125 objects (3 first-time measurements), as well as line-of-sight velocity dispersions for 112 targets (89 first-time measurements). Based on these estimates we derived dynamical mass and mass-to-light ratio estimates by combining the new kinematical information with structural parameters (mostly obtained from HST imaging) and photometric measurements from the literature.

We briefly summarize our results as follows:

- At intermediate GC masses ( $10^5 \lesssim \mathcal{M}_{\text{dyn}}/M_{\odot} \lesssim 10^6$ ) we find the expected population of “classical” GCs, with no anomalous kinematical results. These GCs resemble those of the Local Group in every way, albeit being slightly brighter than average due to our sample selection bias.
- At the high-mass end ( $\mathcal{M}_{\text{dyn}} \gtrsim 10^6 M_{\odot}$ ), we find at least two distinct star-cluster populations in the  $\Upsilon_V^{\text{dyn}}\text{-}\mathcal{M}_{\text{dyn}}$  plane which are well approximated by power-laws of the form  $\Upsilon_V^{\text{dyn}} \propto \mathcal{M}_{\text{dyn}}^{\alpha}$ .
  - The “DGTO sequence” is comprised of objects with  $\mathcal{M}_{\text{dyn}} \gtrsim 2 \cdot 10^6 M_{\odot}$  and  $\Upsilon_V^{\text{dyn}} \lesssim 10 M_{\odot} L_{\odot}^{-1}$  and is well described by a power-law with a slope  $\alpha = 0.33 \pm 0.04$ .
  - The “DSC sequence” objects have  $\mathcal{M}_{\text{dyn}}$  similar to the DGTO sequence clusters, but with a significantly steeper power-law slope,  $\alpha = 0.79 \pm 0.04$ . Moreover, the faint magnitudes ( $M_V \gtrsim -8.5$  mag) lead to anomalously high ( $\Upsilon_V^{\text{dyn}} \geq 6 M_{\odot} L_{\odot}^{-1}$ ) mass-to-light ratios. We point out that at least two LMC GCs (NGC 1754 and NGC 2257) also appear to follow this relation.

Despite being among the brightest clusters of our sample, some DGTO sequence objects show relatively high mass-to-light ratios in the range  $5 \lesssim \Upsilon_V^{\text{dyn}}/M_{\odot} L_{\odot}^{-1} \lesssim 10$ , which require explanation if a non-baryonic mass component is to be avoided. We find that extreme rotation and/or dynamically out of equilibrium configurations can explain their kinematics as well as indications of higher levels of rotational support with increasing  $\mathcal{M}_{\text{dyn}}$ . Plausible alternative and/or concurrent explanations also include particularly top- or bottom-heavy IMFs, or the dynamical influence of central IMBHs. Altogether we consider that these objects represent the very bright tail of the GCLF which is well represented around NGC 5128, but poorly populated in the Local Group.

While the DGTO sequence has a fairly pedestrian explanation, the  $6 \lesssim \Upsilon_V^{\text{dyn}}/M_{\odot} L_{\odot}^{-1} \lesssim 70$  values of the DSC sequence objects are much more difficult to reconcile with the DGTO branch scenarios, save for a small subset. We investigated in detail (see Appendix, for details) the potential impact

of observational, low S/N, and/or instrumental effects on artificially inflating the DSC values, and found that astrophysical explanations are required.

For most of these objects the average stellar velocities (*vis-à-vis* the observed  $\sigma_0$  values) do not appear to be high enough for extreme rotation to explain their dynamics, and if they were, then the clusters would be unstable against rotational break-up. Moreover, it is highly unlikely that all clusters would have their rotation axes aligned with the plane of the sky (assuming  $\sin i \in U[0, 1]$ ), as would be needed to reproduce and minimize the scatter in the observed  $\Upsilon_V^{\text{dyn}}$  vs.  $\mathcal{M}_{\text{dyn}}$  relation. Combined with the difficulty in explaining a mechanism that would impart and maintain the necessary angular momentum for such large rotational velocities, we thus consider extreme rotation/significantly out-of-equilibrium dynamical configurations insufficient and unlikely to explain their properties.

We considered the plausibility of central IMBHs and a central accumulation of dark stellar remnants, consisting of stellar-mass BHs and neutron stars, to be driving the extreme dynamics of the DSC clusters. If they exist, then putative central IMBHs and remnant population can plausibly influence enough of the stars in many of the DSC clusters to provide an explanation for their velocity dispersion measurements. In fact, if our assumed canonical structural profiles were sufficiently perturbed by an IMBH’s presence and/or stellar remnant population, then this explanation requires even less massive IMBHs to become plausible. With that said, given that the IMBH + stellar remnant interpretation can only account for the dynamics of  $\sim 50\%$  of these objects, this is unlikely to explain the emergence of the DSC sequence.

If central IMBHs and stellar remnant populations are not the only cause of the elevated  $\Upsilon_V^{\text{dyn}}$ , then the possibility of significant dark matter mass components must be considered, despite the wide acceptance that “classical” GCs are devoid of DM. This result would have important implications for GC formation models and early structure formation, and indicate that not all extragalactic star clusters are genuine GCs. More importantly, the presence of such amounts of DM in the DSC sequence objects would imply that they represent the lowest mass primordial dark matter halos that have survived accretion onto larger-scale structures to the present day. In other words, there may still exist a large reservoir of  $10^5 M_{\odot}$ -scale dark matter halos surviving in relative isolation in the universe today, at least around relatively quiescent larger dark matter halos like NGC 5128. Moreover, if these objects are stripped of formerly more massive dark matter halos, presumably as former dwarf galaxies, this would imply the presence of a significant collection of objects with  $10^7 \lesssim \mathcal{M}_{\text{dyn}}/M_{\odot} \lesssim 10^8$ , and  $100 \lesssim \Upsilon_V^{\text{dyn}}/M_{\odot} L_{\odot}^{-1} \lesssim 1000$  in the relatively recent past of NGC 5128.

This interpretation is not without its serious problems. For example, with the above properties, central ( $\sim 10$  pc) DM masses/densities on the order of  $\sim 10^3 \times$  larger than canonical DM halo profiles would be required; a scenario that cannot be reconciled with any current theoretical framework. Given the improbability that such massive central BHs, exotic and ultra-concentrated DM halos, or extremely out-of-equilibrium dynamical configurations can individually explain the properties of the DSC sequence objects, it seems perhaps most likely that a mixed bag of such factors may be at play behind this result, although it is puzzling how a combination of these physical mechanisms would conspire to generate a relatively sharp

$\Upsilon_V^{\text{dyn}}$  vs.  $\mathcal{M}_{\text{dyn}}$  relation.

It remains to be seen if similar objects exist in the star cluster systems of other galaxies, but verification of these results will be difficult for more distant systems due to their intrinsic low luminosities. Nonetheless, detailed chemical abundance studies of these objects will shed light on the origins (e.g. primordial or not, simple or multi-generational stellar populations, etc.) of both DGTO and DSC clusters. While the proximity of NGC 5128 provides the possibility to study the internal dynamics and stellar populations of its CSSs, the distance approaches the limits of what is currently feasible with today’s instrumentation on 8-10m class telescopes. Nonetheless, large-scale, complete studies of the chemo-dynamics of GCs in the Local Group, and of giant galaxies within  $\sim 5$  Mpc, will help reveal the true nature of this enigmatic new type of compact stellar systems.

We wish to thank Andres Jordán for providing us with

$r_h$  measurements based on *Hubble Space Telescope* observations prior to publication, and Tim-Oliver Husser for his help with the latest version of the PHOENIX library. We thank Roberto Muñoz, Mia Bovill, Jincheng Yu, Simon Ángel, Rory Smith, Graeme Candlish, Steffen Mieske, and Pavel Kroupa for fruitful discussions and comments that served to improve the manuscript. We also extend our gratitude to the anonymous referee for constructive criticisms that significantly improved this work. This research was supported by FONDECYT Regular Project Grant (No. 1121005) and BASAL Center for Astrophysics and Associated Technologies (PFB-06). M.A.T. acknowledges the financial support through an excellence grant from the “Vicerrectoría de Investigación” and the Institute of Astrophysics Graduate School Fund at Pontificia Universidad Católica de Chile and the European Southern Observatory Graduate Student Fellowship program. M.G. acknowledges financial support through Project “Nucleo de Astronomía”, Universidad Andres Bello.

*Facilities:* Very Large Telescope:Kueyen (FLAMES), HST (ACS), Magellan:Baade (IMACS).

## APPENDIX

### TESTING FOR POTENTIAL DATA ANALYSIS BIASES

We investigated the potential of erroneous literature measurements giving rise to the DSC sequence in Figure 6, and find that one object may be explained by discrepancies found in the literature. For GC 0225, we took the apparent magnitude  $V = 19.93$  mag from the Woodley et al. (2007) catalogue, which is 2.86 magnitudes fainter than in the discovery publication of Holland et al. (1999). We do not attempt to explain this discrepancy, but note that if the brighter measurement is used, it leads to  $\Upsilon_V^{\text{dyn}}$  a factor of  $\sim 14$  lower, bringing it more in line with the DGTO sequence. Additionally, Mieske et al. (2013) note an inconsistency in the size measured by Holland et al. (1999), suggesting that  $r_h$  is  $\sim 3.8\times$  smaller than originally estimated. The smaller size would naturally lower  $\Upsilon_V^{\text{dyn}}$  by the same factor, bringing it more in line with the two intermediate (but still  $\gtrsim 10$ )  $\Upsilon_V^{\text{dyn}}$  clusters. If GC 0225 is both brighter and smaller, then its  $\Upsilon_V^{\text{dyn}}$  would approach one. Eliminating it from the power-law fit results in virtually the same slope ( $\alpha = 0.78 \pm 0.06$ ), with slightly larger scatter.

We also tested for various data reduction effects that may artificially give rise to the DGTO and DSC sequences. For example, a straight-forward explanation is that in performing the convolutions to estimate  $\sigma_{\text{ppxf}}$ , the *ppxf* code may have “jumped” over the targeted Mgb and Fe 5270 spectral features and based the kinematics on the wrong combination of spectral lines due to the relatively low-S/N of some spectra. This explanation would require an error on  $v_{r,\text{ppxf}}$  of  $\gtrsim 100$  km s $^{-1}$  which Figure 4 indicates is not present in our data. Still, given that multiple  $v_r$  measurements can be found in the literature for many of our sample GCs, we individually investigated the DSC sequence objects to search for any literature  $v_r$  estimates that are discrepant by  $\gtrsim 100$  km s $^{-1}$ . We found only three such clusters (GC 0115, GC 0225, and GC 0437 by  $\Delta v_{r,\text{max}} = 142, 93,$  and  $110$  km s $^{-1}$ , respectively), noting that they each fall within the error bars of at least one literature value. Nonetheless, even if all of three GCs are omitted from the fit shown in Figure 6, the relation again does not change significantly ( $\alpha = 0.78 \pm 0.06$ ).

### TESTING FOR TARGET CONFUSION

The significant luminosity difference between the DGTO and DSC sequence GCs calls for investigations into whether the bifurcation is due to observational effects. In general, it is unlikely that any contamination of the sampled GC flux by other sources would produce two such relations, instead of just increased scatter. However, to address this issue we have visually inspected all available archival *HST* imaging data for any potential contamination of the DSC sequence GCs and found no indications for any target confusion due to foreground starlight, background galaxies, or enhanced surface brightness fluctuations of the surrounding galaxy light for each GC.

### TESTING FOR SPURIOUS RESULTS DUE TO NOISY SPECTRA

The well-defined DSC relation could be due to the observational limit of our data. The solid black line shown in Figure 6 shows where GCs with  $M_V = -7.4$  mag (the faintest measured objects in our sample) would lie. Objects to the left are inaccessible to our survey, and the nearly parallel alignment of this line to the DSC sequence suggests that the small scatter may be an artifact of this limit. Indeed, the left panel of Figure 12 shows  $\sigma_{\text{ppxf}}$  as a function of  $M_V$  for our entire sample with symbols as in Figure 6, but GCs with unreliable  $\sigma_{\text{ppxf}}$  shown as open grey circles, and the inset histogram showing the  $M_V$  distribution of GCs for which *ppxf* could not derive a  $\sigma_{\text{ppxf}}$  estimate. It can be seen that most objects with poor/unavailable  $\sigma_{\text{ppxf}}$  encroach upon the luminosities of the DSC sequence. These objects are possibly “classical” GCs with absorption features too narrow for GIRAFFE to resolve, and/or for *ppxf* to accurately measure through the noise, whereas DSC objects have features sufficiently broadened to be measurable. This effect would give the false impression that almost all objects of  $M_V \gtrsim -8.0$  mag seem to have anomalously high  $\Upsilon_V^{\text{dyn}}$ . In fact, the objects on the DSC sequence (red squares) show a trend of higher luminosity with larger  $\sigma_{\text{ppxf}}$ , contrary

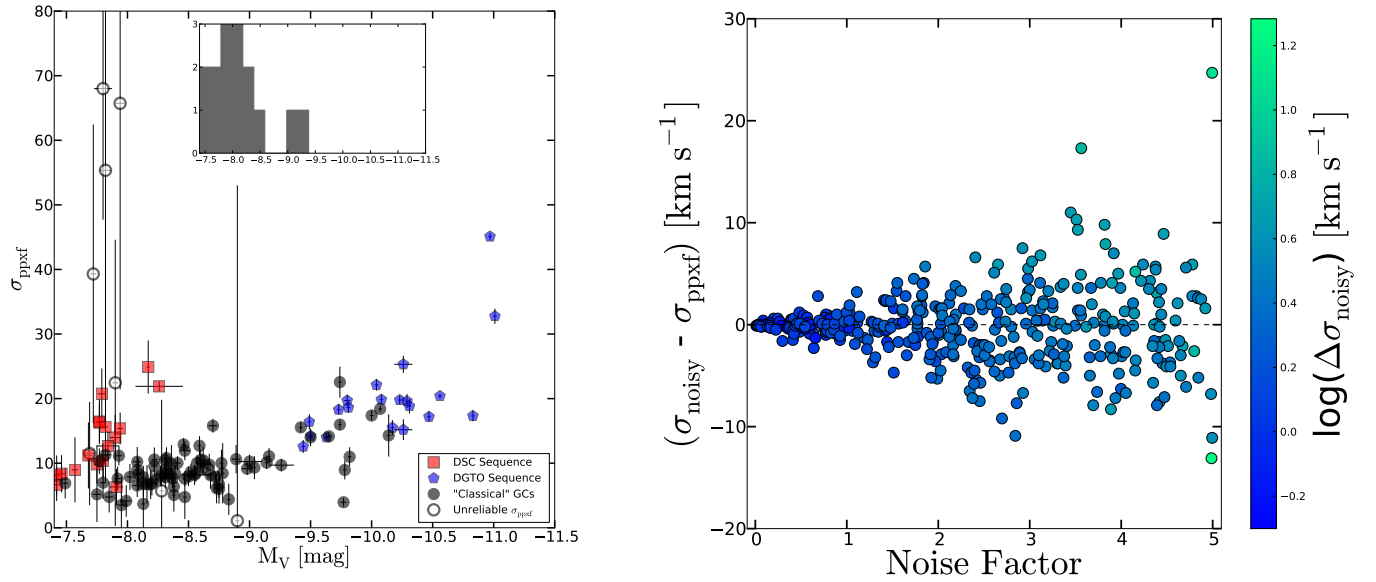


FIG. 12.— (Left panel):  $\sigma_{ppxf}$  values as a function of  $M_V$ , with brightness increasing to the right. Symbol shapes are as in Figure 6, with the addition of objects for which  $\sigma_{ppxf}$  could not be estimated (grey inset histogram) or which we considered unreliable (open grey circles). (Right panel): Difference between velocity dispersion measured on spectra with artificially added noise,  $\sigma_{noisy}$ , and our measurements,  $\sigma_{ppxf}$ , as a function of the amount of noise added in units of the standard deviation of the original spectra. The errors of the  $\sigma_{noisy}$  measurements are shown on a logarithmic scale, parametrized by the color shading to illustrate the increased uncertainties as more noise is added. If poor-quality spectra were the cause of the DSC sequence, an upturn of the  $\sigma_{noisy} - \sigma_{ppxf}$  difference would be expected towards larger noise factors; however, the symmetric increase in spread to both negative and positive  $\sigma_{noisy} - \sigma_{ppxf}$  values clearly rules out this possibility.

to the expectation if noise were ‘‘washing-out’’ the finer spectral details used to estimate  $\sigma_{ppxf}$ .

Since the DSC sequence objects are among the faintest objects in our sample (see Figure 7), an obvious point of concern is that their spectra are among the noisiest. We therefore performed the following test to check against the potential of noise ‘‘washing out’’ some of the finer spectral details used to estimate  $\sigma_{ppxf}$ , thus tricking the code into estimating systematically wider dispersions. We took four DGTO sequence GCs (GC 0106, GC 0277, GC 0306 and GC 0310; chosen to cover a reasonable luminosity range), artificially added varying levels of noise, and repeated the  $\sigma_{ppxf}$  measurements. For each GC we added noise, pixel by pixel, by randomly drawing from a  $N(0, n \cdot \sigma_{spec})$  distribution where  $\sigma_{spec}$  is the flux dispersion intrinsic to each spectrum, and  $n$  is drawn from  $U(0, 5)$  distributions. This procedure decreases the spectral S/N by a factor  $1/n$ . Repeating this process 100 times for each GC then builds a picture of how well behaved the *ppxf* code is for increasingly noisy spectra. The right panel of Figure 12 shows the results of this exercise for all four GCs and it is clear that even for large amounts of noise, the points cluster well around the adopted  $\sigma_{ppxf}$  values, with increased dispersion bracketing the nominal values accompanied by larger errors. If sudden ‘‘jumps’’ in  $\sigma_{ppxf}$  due to noisy spectra were the cause of the elevated  $\Upsilon_V^{dyn}$  shown by the DSC sequence, then it would be expected that the points in Figure 12 would tend towards higher  $\sigma_{noisy}$  estimates with stronger amplified noise. No hint of such asymmetric trend is seen in the plot, and we conclude that the DSC sequence is not artificially created by poor quality spectra.

#### TESTING FOR CORRELATIONS WITH GALACTOCENTRIC RADIUS AND AZIMUTHAL ANGLE

In searching for the origins of the structures found in Figure 6, in particular the bifurcation at high  $\mathcal{M}_{dyn}$ , we test whether any correlation of the measured  $\sigma_{ppxf}$  with spatial distribution might give deeper insight into our results. For the following, we note that we are using the raw  $\sigma_{ppxf}$  measurement directly obtained from the spectra without subsequent correction for GC light profile sampling. We plot in Figure 13  $\sigma_{ppxf}$  as functions of galactocentric radius ( $R_{gc}$ ; left panel), and azimuthal angle ( $\Phi$ ; right panel), where  $0^\circ$  corresponds to north and  $\Phi$  increases clockwise. We find no indications for any  $\sigma_{ppxf} - R_{gc}$  or  $\sigma_{ppxf} - \Phi$  correlations for our GC sample. More importantly, we find no such correlations for either of the GC sub-samples, in particular for the DSC GCs (red squares). We conclude that systematic variations in  $\sigma_{ppxf}$  as a function of spatial distribution are not responsible for the bifurcation in the  $\Upsilon_V^{dyn} - \mathcal{M}_{dyn}$  relation.

#### TESTING FOR GALAXY SURFACE BRIGHTNESS CONTAMINATION

Here we investigate the fractional flux from NGC 5128’s diffuse galaxy light component that enters each fibre together with the GC light. We consider the potential impact of such fibre contamination, which could potentially lead the *ppxf* code to predict artificially high  $\sigma_{ppxf}$  values. However, if this was the case, one would expect that the associated error bars would reflect this uncertainty (given full error propagation), and/or that the elevated  $\Upsilon_V^{dyn}$  values required to explain the DSC sequence (see §4.2) would either tend towards *higher* values with *decreasing* luminosity, which is not seen in our data (see Figure 7 and 11), or that

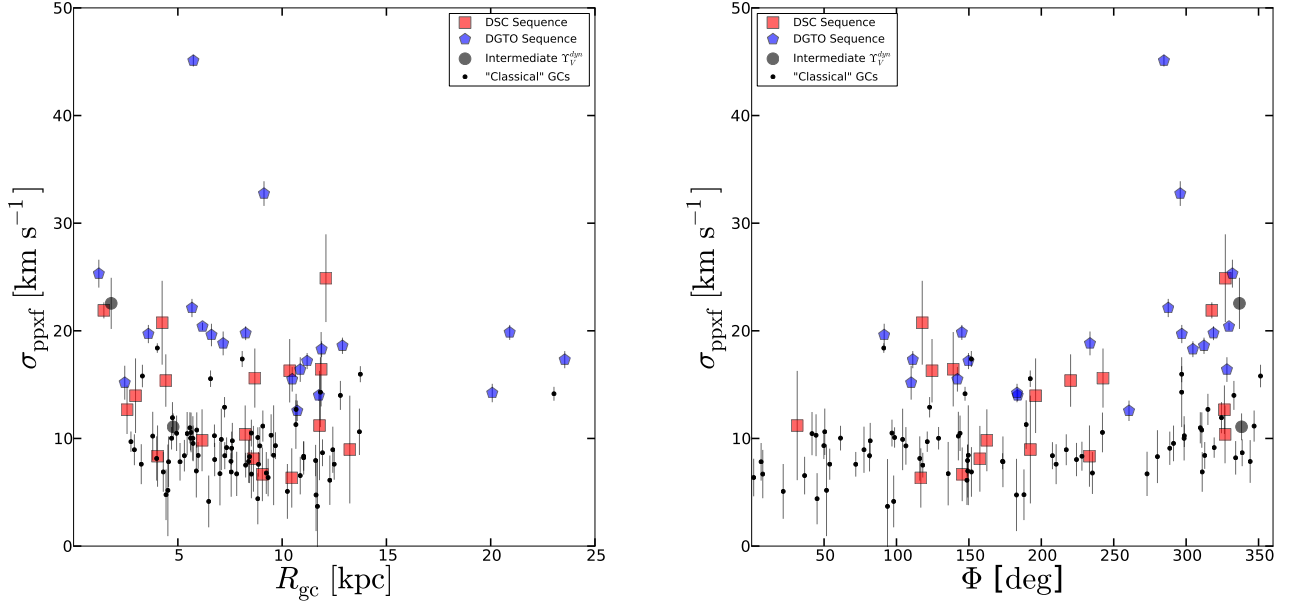


FIG. 13.— (Left panel): Raw  $\sigma_{\text{ppxf}}$  measurement shown as a function of galactocentric radius,  $R_{\text{gc}}$ , with symbols as in Figures 6 and 7. (Right panel): Same as in the left panel, but showing  $\sigma_{\text{ppxf}}$  as a function of azimuthal angle, with  $0^\circ$  corresponding to North and increasing clockwise (see also Figure 1). No obvious correlations between  $\sigma_{\text{ppxf}}$ ,  $R_{\text{gc}}$ , or  $\Phi$  are seen, effectively ruling out the possibility of systematic variations of  $\sigma_{\text{ppxf}}$  with spatial distribution giving rise to the DGTO or DSC sequences.

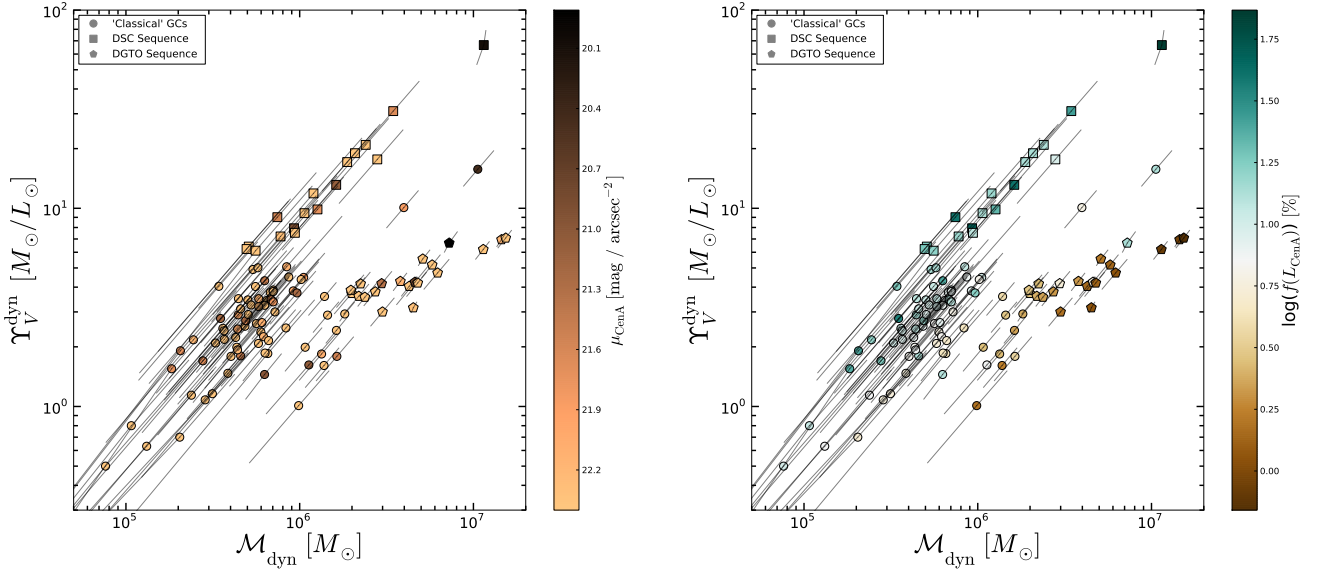


FIG. 14.—  $\Upsilon_V^{\text{dyn}}-\mathcal{M}_{\text{dyn}}$  plane as in Figure 6, but now in the left panel with the local NGC 5128 surface brightness parametrizing the data point color, and in the right panel with the decadal logarithm of the fractional NGC 5128 galaxy light contribution to each of the sampled GC fluxes, *before* sky subtraction.

there would be a vanishing or no  $\Upsilon_V^{\text{dyn}}-\mathcal{M}_{\text{dyn}}$  correlation at all. As can be seen in Figure 6, the DSC sequence is consistent with the individual error bars, which themselves are dominated by the fully propagated uncertainties on  $\sigma$ .

Given that our background light SED modeling and subsequent subtraction from each fibre is not a localized process (see § 2.3), visual inspection of the sky+background subtracted GC spectra indicated that they should not be significantly affected by residual galaxy light contamination. To be sure, we explicitly calculated the expected residuals by comparing the difference between the flux of NGC 5128 at the location of each target and our final sky estimates to the flux of our final target spectra. The results suggested that residual components due to diffuse galaxy light is for all GCs  $< 4\%$ , and in most cases near the 1% level, with the expected trend toward lower residuals with increasing  $R_{\text{gc}}$ . We then tested for the maximal effects of these residuals on the DSC sequence objects by adding the signal from the nearest sky fibre to the final, reduced target spectra at flux levels between 1% and 90% of the object flux and re-measuring  $\sigma_{\text{ppxf}}$ . The results showed that below  $\sim 20\%$ , the effect on  $\sigma_{\text{ppxf}}$  was

negligible, above which  $\sigma_{\text{ppxf}}$  monotonically growing with increased sky contamination, as one would expect.

In any case, we plot in the left panel of Figure 14 the  $\Upsilon_V^{\text{dyn}}-\mathcal{M}_{\text{dyn}}$  plane, as in Figure 6, but parameterize the data point color this time with the local surface brightness of NGC 5128 at each GC location. We obtain the surface brightness values from the profiles measured as part of the Carnegie-Irvine Galaxy Survey (CGS; see Ho et al. 2011; Li et al. 2011). No obvious correlations with local surface brightness values are found that would drive the bifurcation in the  $\Upsilon_V^{\text{dyn}}-\mathcal{M}_{\text{dyn}}$  relation. We continue by using the surface brightness profile for NGC 5128 to compute the fractional background flux,  $f(L_{\text{CenA}})$ , entering each fibre with the GC fluxes. The right panel of Figure 14 shows the results, with color parameterized by  $\log f(L_{\text{CenA}})$  before any sky+background subtraction is performed. Several results are shown: 1) The “classical” and DGTO sequence GCs reveal the expected correlation between GC mass (i.e. luminosity) and  $f(L_{\text{CenA}})$  with a decreasing  $f(L_{\text{CenA}})$  sequence from  $\sim 30\%$  for the low-mass GCs to negligible fractions for the highest-mass clusters; 2) GCs on the DSC sequence show on average larger  $f(L_{\text{CenA}})$  than GCs on the DGTO sequence as expected from the trends seen in Figure 7, which shows that DSC GCs have luminosities of  $-8.5 \lesssim M_V \lesssim -7.5$  mag; 3) The DSC sequence GCs show *no* correlation between  $f(L_{\text{CenA}})$  and  $\Upsilon_V^{\text{dyn}}$  or  $\mathcal{M}_{\text{dyn}}$ , in contrast to the expectation if the  $\Upsilon_V^{\text{dyn}}-\mathcal{M}_{\text{dyn}}$  sequences were created by insufficient background light subtraction.

While Figure 14 illustrates fibre contamination before any sky modeling and subtraction was carried out, we performed one final test to check for the worst effect that insufficient background subtraction could have. We first identified higher-S/N GCs with  $\sigma_{\text{ppxf}}$  equivalent to that which would give a “normal”  $\Upsilon_V^{\text{dyn}}$  for a DSC sequence cluster. For example, given the DSC GC 0324’s  $\sigma_{\text{ppxf,GC 0324}} = 24.89 \text{ km s}^{-1}$  and  $\Upsilon_{V,\text{GC 0324}}^{\text{dyn}} = 14.07 M_{\odot} L_{\odot}^{-1}$ , we identified the DGTO GC 0050 with  $\sigma_{\text{ppxf,GC 0050}} = 10.09 \text{ km s}^{-1}$ , which would give  $\Upsilon_{V,\text{GC 0324}}^{\text{dyn}} = 2.31 M_{\odot} L_{\odot}^{-1}$ . Using three such combinations, we scaled the individual spectra of the bright GC, pre-sky subtraction, to the flux level of the fainter cluster, and added the nearest sky fibre’s signal. Performing the sky subtraction as before (see § 2.3) with the next three closest fibres then simulated the noise levels of the faint GC, but preserved the spectral details of the brighter. Measuring  $\sigma_{\text{ppxf}}$  on the degraded spectrum was, at worst, consistent with our adopted measurements, and even led to a slightly lower  $\sigma_{\text{ppxf}}$  for two of the experiments. We conclude that improper background subtraction is thus very unlikely to inflate our  $\sigma_{\text{ppxf}}$  measurements of the DSC sequence objects.

#### REFERENCES

- Ashman, K. M., & Zepf, S. E. 1998, *Globular Cluster Systems* (Cambridge, UK: New York : Cambridge University Press)
- Ashman, K. M., & Zepf, S. E. 2008, *Globular Cluster Systems*, (Cambridge, UK: Cambridge University Press)
- Banerjee, S., & Kroupa, P. 2011, *ApJ*, 741, L12
- Barmby, P., Holland, S.T., & Huchra, J.P. 2002, *AJ*, 123, 1937
- Barmby, P., McLaughlin, D.E., Harris, W.E., Harris, G.L., & Forbes, D.A. 2007, *AJ*, 133, 2764
- Beasley, M.A., Bridges, T., Peng, E., et al. 2008, *MNRAS*, 386, 1443
- Bedin, L.R., Piotto, G., Anderson, J., et al. 2004, *ApJ*, 605, 125
- Belokurov, V., Zucker, D. B., Evans, N. W., et al. 2007, *ApJ*, 654, 897
- Bianchini, P., Varri, A. L., Bertin, G., & Zocchi, A. 2013, *ApJ*, 772, 67
- Binney, J., & Tremaine, S. (ed.) 2008, *Galactic Dynamics* (2nd ed.; Princeton, NJ: Princeton Univ. Press)
- Brown, T. M., Tumlinson, J., Geha, M., et al. 2012, *ApJ*, 753, L21
- Burstein, D., Faber, S. M., Gaskell, C. M., & Krumm, N. M. 1984, *ApJ*, 287, 586
- Cappellari, M., & Emsellem, E. 2004, *PASP*, 116, 138
- Carlberg, R. G. 2009, *ApJ*, 705, L223
- Carlberg, R. G., Richer, H. B., McConnachie, A. W., et al. 2011, *ApJ*, 731, 124
- Carlberg, R. G., & Grillmair, C. J. 2013, *ApJ*, 768, 171
- Chilingarian, I. V., Mieske, S., Hilker, M., & Infante, L. 2011, *MNRAS*, 412, 1627
- Colucci, J. E., Durán, M. F., Bernstein, R.A., & McWilliam, A. 2013, *ApJ*, 773, L36
- Conroy, C., Loeb, A., & Spergel, D. N. 2011, *ApJ*, 741, 72
- Dabringhausen, J., Hilker, M., & Kroupa, P. 2008, *MNRAS*, 386, 864
- Dabringhausen, J., Kroupa, P., & Baumgardt, H. 2009, *MNRAS*, 394, 1529
- Davies B., Figer, D. F., Kudritzki, R. P., et al. 2007, *ApJ*, 671, 781
- De Lucia, G., Springel, V., White, S. D. M., Croton, D., & Kauffmann, G. 2006, *MNRAS*, 366, 499
- De Lucia, G., & Blaizot, J. 2007, *MNRAS*, 375, 2
- Djorgovski, S. 1995, *ApJ*, 438, L29
- Djorgovski, S. G., Gal, R. R., McCarthy, J. K., et al. 1997, *ApJ*, 474, L19
- Fabricius, M. H., Noyola, E., Rukdee, S., et al. 2014, *ApJ*, 787, L26
- Figer D. F., McLean, I. S., & Morris, M. 1999, *ApJ*, 514, 202
- Fusi Pecci, F., Battistini, P., Bendinelli, O., et al. 1994, *A&A*, 284, 349
- Garrison-Kimmel, S., Boylan-Kolchin, M., Bullock, J. S., & Kirby, E. N. 2014, *MNRAS*, 444, 222
- Georgiev, I. Y., Puzia, T. H., Goudfrooij, P., & Hilker, M. 2010, *MNRAS*, 406, 1967
- Gieles, M., Portegies Zwart, S. F., Baumgardt, H., et al. 2006, *MNRAS*, 371, 793
- Gilmore, G., Wilkinson, M. I., Wyse, R. F. G., et al. 2007, *ApJ*, 663, 948
- Gnedin, O. Y., & Ostriker, J. P. 1997, *ApJ*, 474, 223
- Gualandris, A., & Merritt, D. 2008, *ApJ*, 678, 780
- Harayama Y., Eisenhauer, F., & Martins, F. 2008, *ApJ*, 675, 1319
- Harris, G. L. H., Hesser, J. E., Harris, H. C. & Curry, P. J. 1984, *ApJ*, 287, 175
- Harris, W. E. 1991, *ARA&A*, 29, 543
- Harris, G. L. H., Geisler, D., Harris, H. C., & Hesser, J.E. 1992, *AJ*, 104, 613
- Harris, G. L. H., Harris, W. E., & Poole, G. B. 1999, *AJ*, 117, 855
- Harris, G. L. H., & Harris, W. E. 2000, *AJ*, 120, 2423
- Harris, W. E., & Harris, G. L. H. 2002, *AJ*, 123, 3108
- Harris, W. E., Harris, G. L. H., Holland, S. T., & McLaughlin, D. E. 2002a, *AJ*, 124, 1435
- Harris, G. L. H., Geisler, D., Harris, W. E., & Hesser, J. E. 2002b, in *IAU Symp. 207, Extragalactic Star Clusters*, ed. D. P. Geisler, E. K. Grebel, & D. Minniti (San Francisco, CA: ASP), 309
- Harris, G. L. H., Rejkuba, M., & Harris, W. E. 2010, *PASA*, 27, 457
- Harris, G. L. H., Gómez, M., Harris, W. E., et al. 2012, *AJ*, 143, 84
- Haşegan, M., Jordán, A., Côté, P., et al. 2005, *ApJ*, 627, 203
- Hesser, J. E., Harris, H. C., van den Bergh, S., & Harris, G. L. H. 1984, *AJ*, 276, 491
- Hesser, J. E., Harris, H. C., & Harris, G. L. H. 1986, *ApJ*, 303, L51
- Hilker, M., Baumgardt, H., Infante, L., et al. 2007, *A&A*, 463, 119
- Ho, L. C., Li, Z.-Y., Barth, A. J., Seigar, M. S., & Peng, C. Y. 2011, *ApJS*, 197, 21
- Holland, S., Fahlman, G. G., & Richer, H. B. 1997, *AJ*, 114, 1488
- Holland, S., Côté, P., & Hesser, J. E. 1999, *A&A*, 348, 418
- Husser, T.-O., von Berg, S. W., Dreizler, S., et al. 2013, *A&A*, 553, 6
- Ibata, R., Nipoti, C., Sollima, A., et al. 2013, *MNRAS*, 428, 3648
- Kacharov, N., Bianchini, P., Koch, A., et al. 2014, *A&A*, 567, 69
- King, I. R. 1966, *AJ*, 71, 64
- Kissler-Patig, M., Jordán, A., & Bastian, N. 2006, *A&A*, 448, 1031
- Komossa, S., & Merritt, D. 2008, *ApJ*, 689, L89
- Koss, M., Blecha, L., Mushotzky, R., et al. 2014, *MNRAS*, 445, 515
- Krauss, L. M., & Chaboyer, B. 2003, *Science*, 299, 65
- Krujissen, J. M. D. & Lützgendorf, N. 2013, *MNRAS*, 434, L41
- Lanzoni, B., Mucciarelli, A., Origlia, L., et al. 2013, *ApJ*, 769, 107
- Leigh, N. W. C., Lützgendorf, N., Geller, A. M., et al. 2014, *MNRAS*, 444, 29
- Liu, J., et al. 2011, *ApJS*, 192, 10L
- Li, Z.-Y., Ho, L. C., Barth, A. J., & Peng, C. Y. 2011, *ApJS*, 197, 22

- Lotz, J. M., Telford, R., Ferguson, H. C., et al. 2001, *ApJ*, 552, 572
- Lützgendorf, N., Kissler-Patig, M., Noyola, E., et al. 2011, *A&A*, 533, AA36
- Madau, P. & Quataert, E. 2004, *ApJ*, 606, L17
- Malin, D. R., Quinn, P. J., & Graham, J. A. 1983, *ApJ*, 272, L5
- Marchesini, D., Muzzin, A., Stefanon, M., et al. 2014, *arXiv:1402.0003v1*
- Marleau, F. R., Graham, J. R., Liu, M. C., & Charlot, S. 2000, *AJ*, 120, 1779
- Martini, P., & Ho, L. C. 2004, *ApJ*, 610, 233
- McConnachie, A. W., Irwin, M. J., Ibata, R. A., et al. 2009, *Nature*, 461, 66
- McLaughlin, D. E. 2000, *ApJ*, 539, 618
- McLaughlin, D. E., & van der Marel, R. P. 2005, *ApJS*, 161, 304
- McLaughlin, D. E., & Fall, S. M. 2008, *ApJ*, 679, 1272
- Merritt, D. 2004, *Coevolution of Black Holes and Galaxies*, Vol. 1 (Cambridge, UK: Cambridge Univ. Press)
- Merritt, D., Milosavljević, M., Favata, M., Hughes, S. A., & Holz, D. E. 2004, *ApJ*, 607, L9
- Merritt, D., Schnittman, J. D., & Komossa, S. 2009, *ApJ*, 699, 1690
- Meylan, G., Sarajedini, A., Jablonka, P., et al. 2001, *AJ*, 122, 830
- Mieske, S., Hilker, M., Infante, L., & Jordán, A. 2006, *AJ*, 131, 2442
- Mieske, S., Hilker, M., Jordán, A., et al. 2008, *A&A*, 487, 921
- Mieske, S., & Kroupa, P. 2008, *ApJ*, 677, 276
- Mieske, S., Frank, M. J., Baumgardt, H., et al. 2013, *A&A*, 558, 14
- Mood, A. M. 1950, *Introduction to the Theory of Statistics* (McGraw-Hill), 394-399
- Moore, B. 1996, *ApJ*, 461, L13
- Norris, J. E., & Da Costa, G. S. 1995, *A&A*, 447, 680
- Pancino, E., Pasquini, L., Hill, V., Ferraro, F. R., & Bellazzini, M. 2002, *ApJ*, 568, L101
- Peebles, P. J. E. 1984, *ApJ*, 277, 470
- Peng, E. W., Ford, H. C., Freeman, K. C., & White, R. L. 2002, *AJ*, 124, 3144
- Peng, E. W., Ford, H. C., & Freeman, K. C. 2004, *ApJ*, 602, 705
- Peng, E. W., Jordán, A., Côté, P., et al. 2008, *ApJ*, 681, 197
- Pfalzner S. 2009, *A&A*, 498, L37
- Piotto, G. 2008, *Mem. Soc. Astron. Ital.*, 79, 334
- Piotto, G. 2008, in *IAU Symp. 246, Dynamical Evolution of Dense Stellar Systems Proceedings*, ed. Vesperini, E., Giersz, M., & Sills, A. (Cambridge, UK: Cambridge Univ. Press), 258
- Portegies Zwart, S. F., McMillan, S. L. W., & Gieles, M. 2010, *ARA&A*, 48, 431
- Puzia, T. H., Paolillo, M., Goudfrooij, P., et al. 2014, *ApJ*, 786, 78
- Rashkov, V., & Madau, P. 2014, *ApJ*, 780, 187
- Rejkuba, M., Minniti, D., Silva, D., & Bedding, T. 2003, *A&A*, 411, 351
- Rejkuba, M., Dubath, P., Minniti, D., & Meylan, G. 2007, *A&A*, 469, 147
- Rejkuba, M., Harris, W. E., Greggio, L., & Harris, G. L. H. 2011, *A&A*, 526, A123
- Ricotti, M. 2003, *MNRAS*, 344, 1237
- Safonova, M., & Shastri, P. 2010, *Ap&SS*, 325, 47
- Saitoh, T. R., Koda, J., Okamoto, T., Wada, K., & Habe, A. 2006, *ApJ*, 640, 22
- Sawala, T., Frenk, C. S., Fattahi, A., et al. 2014, *arXiv:1406.6362*
- Schlafly, E. F., & Finkbeiner, D. P. 2011, *ApJ*, 737, 103
- Seth, A., van den Bosch, R., Mieske, S., et al. 2014, *Nature*, 513, 398
- Simon, J. D., & Geha, M. 2007, *ApJ*, 670, 313
- Sinnott, B., Hou, A., Anderson, R., Harris, W. E., & Woodley, K. 2010, *AJ*, 140, 2101
- Smith, R., Sánchez-Janssen, R., Fellhauer, M., et al. 2013, *MNRAS*, 429, 1066
- Smith, R., Fellhauer, M., Candlish, G. N., et al. 2013, *MNRAS*, 433, 2529
- Sollima, A., Bellazzini, M., & Lee, J.-W. 2012, *ApJ*, 755, 156
- Soria, R., Mould, J. R., Watson, A. M., et al. 1996, *ApJ*, 465, 79
- Spitzer, L., Jr. 1969, *ApJ*, 158, L139
- Strader, J., Caldwell, N., & Seth, A. 2011, *AJ*, 142, 8
- Strader, J., Chomiuk, L., Maccarone, T. J., et al. 2012, *ApJ*, 750, L27
- Sun, M.-Y., Jin, Y.-L., Gu, W.-M., et al. 2013, *ApJ*, 776, 118
- Taylor, M. A., Puzia, T. H., Harris, G. L. H., et al. 2010, *ApJ*, 712, 119
- Tollerud, E. J., Bullock, J. S., Graves, G. G., & Wolf, J. 2011, *ApJ*, 726, 108
- van den Bergh, S., Hesser, J. E., & Harris, G. L. H. 1981, *AJ*, 86, 24
- Varri, A. L., & Bertin, G. 2012, *A&A*, 540, A94
- Webb, J. J., Harris, W. E., Sills, A., & Hurley, J. R. 2013, *ApJ*, 764, 124
- White, R. E., & Shawl, S. J. 1987, *ApJ*, 317, 246
- Willman, B., Blanton, M. R., West, A. A., et al. 2005, *AJ*, 129, 2692
- Wolf, J., Martinez, G. D., Bullock, J. S., et al. 2010, *MNRAS*, 406, 1220
- Woodley, K. A., Harris, W. E., & Harris, G. L. H. 2005, *AJ*, 129, 2654
- Woodley, K. A., Harris, W. E., Beasley, M. A., et al. 2007, *AJ*, 134, 494
- Woodley, K. A., Gómez, M., Harris, W. E., Geisler, D., & Harris, G. L. H. 2010, *AJ*, 139, 1871
- Woodley, K. A., Harris, W. E., Puzia, T. H., et al. 2010, *ApJ*, 708, 1335
- Worthey, G., 1994, *ApJS*, 95, 107
- Worthey, G., & Ottaviani, D. L. 1997, *ApJS*, 111, 377
- Zucker, D. B., Belokurov, V., Evans, N. W., et al. 2006, *ApJ*, 650, L41
- Zucker, D. B., Kniazev, A. Y., Martínez-Delgado, D., et al. 2007, *ApJ*, 659, L21